List of Papers

This thesis is based on the following publications:

I. **Isomer spectroscopy of neutron rich $^{190}\mathbf{W}_{116}$**
Zs. Podolyàk, P.H. Regan, M. Pfützner, J. Gerl, M. Hellström, M. Caamaño, P. Mayet, Ch. Schlegel, A. Aprahamian, J. Benlliure, A.M. Bruce, P.A. Butler, D. Cortina Gil, D.M. Cullen, J. Döring, T. Enqvist, F. Rejmund, C. Fox, J. Garcés Narro, H. Geissel, W. Gelletly, J. Giovinazzo, M. Górska, H. Grawe, R. Grzywacz, A. Kleinböhl, W. Korten, M. Lewitowicz, R. Lucas, H. Mach, M. Mineva, C.D. O'Leary, F. De Oliveira, C.J. Pearson, M. Rejmund, M. Sawicka, H. Schaffner, K. Schmidt, Ch. Theisen, P.M. Walker, D.D. Warner, C. Wheldon, H.J. Wollersheim, S.C. Wooding, and F.R. Xu,
Phys. Lett. B **491**, (2000) 225.

II. **Isomer spectroscopy of fragmentation and fission products**
M.N. Mineva, M. Hellström, M. Bernas, J. Gerl, H. Grawe, M. Pfützner, Zs. Podolyák, P. H. Regan, and the GSI Isomer Collaboration,
Proceedings of the 2nd International Balkan School on Nuclear Physics, Bodrum, Turkey, September 2000, Balkan Physics Letters Special Issue (2000), p.267-272.

III. **A new μs isomer in ^{136}Sb produced in projectile fission of ^{238}U**
M.N. Mineva, M. Hellström, M. Bernas, J. Gerl, H. Grawe, M. Pfützner, P.H. Regan, M. Rejmund, D. Rudolph, F. Becker, C.R. Bingham, T. Enqvist, B. Fogelberg, H. Gausemel, H. Geissel, J. Genevey, M. Górska, R. Grzywacz, K. Hauschild, Z. Janas, I. Kojouharov, Y. Kopatch, A. Korgul, W. Korten, J. Kurcewicz, M. Lewitowicz, R. Lucas, H. Mach, S. Mandal, P. Mayet, C. Mazzocchi, J.A. Pinston, Zs. Podolyàk, H. Schaffner, Ch. Schlegel, K. Schmidt, K. Sümmerer, and H.J. Wollersheim,
Eur. Phys. J. **A11** (2001) 9.

IV. **Isomers in the vicinity of ^{132}Sn produced by in-flight fission of ^{238}U**
M.N. Mineva, and the GSI Isomer Collaboration,
Proceedings of the International Symposium on Nuclear Structure Physics, Göttingen, Germany, 5-8 March 2001, p.381-382.

V. **Angular momentum population in the fragmentation of ^{208}Pb at 1 GeV/nucleon**
M. Pfützner, P. H. Regan, P.M. Walker, M. Caamaño, J. Gerl, M. Hellström, P. Mayet, K.-H. Schmidt, Zs. Podolyàk, M.N. Mineva, A. Aprahamian, J. Benlliure, A.M. Bruce, P.A. Butler, D. Cortina Gil, D.M. Cullen, J. Döring, T. Enqvist, C. Fox, J. Garcés Narro, H. Geissel, W. Gelletly, J. Giovinazzo, M. Górska, H. Grawe, R. Grzywacz, A. Kleinböhl, W. Korten, M. Lewitowicz, R. Lucas, H. Mach, C.D. O'Leary, F. De Oliveira, C.J. Pearson, F. Rejmund, M. Rejmund, M. Sawicka, H. Schaffner, Ch. Schlegel, K. Schmidt, Ch. Theisen, F. Vivès, D.D. Warner, C. Wheldon, H.J. Wollersheim, and S.C. Wooding,
Phys. Rev. C **65** (2002), 064604.

VI. **Probing neutron-rich In and Cd nuclei with isomer spectroscopy**
M. Hellström, M.N. Mineva, A. Blazhev, H.J. Boardman, J. Ekman, J. Gerl, K. Gladnishki, H. Grawe, R. Page, Zs. Podolyak, D. Rudolph, and the GSI-FRS-Isomer collaboration,
Proceedings of the XXXII International Workshop on Gross Properties of Nuclei and Nuclear Excitations, Hirschegg, Austria, Jan. 12-18, 2003, H. Feldmeier *et al.* Eds. (2003), p. 72.

American Physical Society
Research Road
Box 9000, Ridge
NY 11961-9000
USA

Elsevier Science B. V.
P. O. Box 103
1000 AC Amsterdam
The Netherlands

Gesellschaft für Schwerionenforschung mbH
Planckstraße 1
D-64291 Darmstadt
Germany

Società Italiana di Fisica and Springer-Verlag
Via Castiglione 101
I-40136 Bologna
Italy

World Scientific Publishing Co. Pte. Ltd.
57 Shelton Street, Covent Garden
London WC2H 9HE
United Kingdom

Acknowledgements

I would like to thank all my colleagues in the Nuclear Structure Group for the very nice physics discussions during the regular group meetings we have had.

In particular I would like to express my sincere gratitude to Prof. Claes Fahlander for giving me the opportunity to join the group and in this way giving me the chance to see, and work with the most modern and advanced experimental nuclear physics facilities. I am grateful to him for always asking questions in a way that inspires deeper insight and understanding of physics, as well as for frequently suggesting me and my fellow students from the group to report the status of our work.

Especially I would like to thank my thesis advisor Dr. Margareta Hellström for her constant effort to explain and help me understand the details of the experimental techniques, and for the nice time spent working together.

I am also very grateful to Dr. Dirk Rudolph for his help and friendly support.

The discussions I have had with the Mathematical Physics group held in the nice atmosphere of coffee and cookies have proven once again that physics can be fun in a relaxed environment.

In addition, I would like to thank all my colleagues from the "GSI Isomer Collaboration" for the friendly teamwork and nice atmosphere during the experiments. My fruitful discussions with Dr. Hubert Grawe are greatly acknowledged.

But most of all, I want to express my gratitude to my family, for understanding me in my aspiration to explore the so abstract to them phenomena of the nuclear structure, and my husband, Nikolay, for the discussions in the light of other fields of physics. I want to thank them for their unconditional support and love.

Contents

Chapter 1

Introduction

Nuclei far from stability have been an interesting and exciting field for both theoretical and experimental studies for many years. Figure 1.1 shows the nuclidic chart. The *line of β-stability* consists of about 270 isotopes, which in their ground state are stable against all nuclear decay modes. More than 2000 unstable isotopes, situated both on the proton- and neutron-rich sides of the β-stability line, have been studied, which has inspired developments of new experimental tools and theoretical models. For several decades, it has been an experimental challenge to reach more and more "exotic" nuclear systems in terms of either the synthesis of super-heavy elements, or producing nuclei with large excess or deficiency of neutrons, to try and get answers to such questions as: What is the shell structure for nuclei far from the β-stability line? Are the known magic numbers the same far from stability? Do the nuclear models developed at or near stability still work, and how good are they for the interpretation of the experimental observables?

The technical progress allowed the limits of nucleon binding, i.e. the *proton and neutron drip lines*, to be reached for many nuclei. On the proton-rich side, a number of nuclei have exhibited prompt proton decay from their ground state, as a proof for having reached the proton drip line. The heaviest of them so far is ^{185}Bi with proton number Z= 83 [1]. For neutrons the drip line is much farther away from the stability than for protons because of the absence of Coulomb repulsion. In fact, only the lightest neutron-drip line nuclei (up to oxygen, Z=8), have been reached so far. In these light neutron-rich nuclei unusual nuclear matter distribution, so called *neutron halo*, has been observed. In nuclei with more than 25 protons the neutron drip line cannot be reached experimentally [2], but nevertheless nuclei with large neutron-proton ratio can be produced. The weak neutron binding, due to the proton-neutron assymetry, implies the existence of a *neutron skin*, i.e., a dramatic excess of neutrons at large distances. The existence of a neutron skin may lead to new vibrational modes in which, for example, the neutron skin oscillates out of phase with a well-bound proton-neutron core [3]. In those nuclei one may have the opportunity to study nearly pure neutron matter in the laboratory.

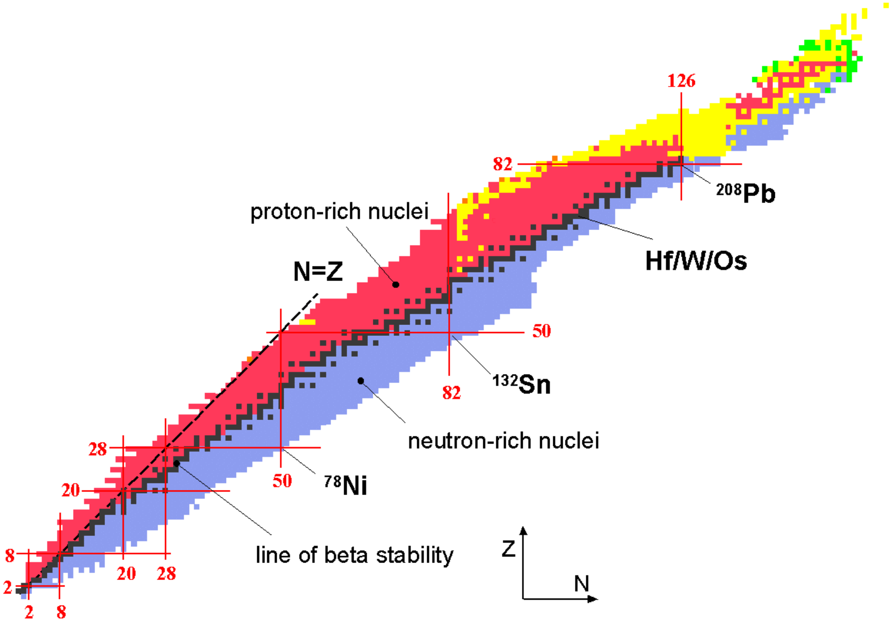

Figure 1.1: The nuclidic chart.

Other phenomena, which are expected to occur in neutron-rich nuclei, are related to the evolution of the shell structure. There are indications that the shell structure changes as one moves towards very neutron-rich nuclei. The disappearance of the $N = 8$ shell and the appearance of a new $N = 16$ shell reported recently [4, 5] is a first confirmation of a re-organization of nuclear shells in regions away from stability.

In Figure 1.1 the nuclei ^{78}Ni, ^{132}Sn, and ^{208}Pb are marked. They are doubly magic nuclei, they are well bound systems, and spherical in their ground states. They play an important role in nuclear structure research. Studying nuclei in their close neighborhood, with only a few valence particles or holes outside the closed shells, is an efficient probe into the general features of the nuclear many-body systems. They provide test on the particle-hole and particle-particle interactions, on the particle-core polarization and excitation modes, and on nuclear deformations. It is interesting to compare the different sets of doubly magic nuclei and their surrounding nuclei, to explore the changes in nuclear structure when different orbitals are occupied and different shells are filled.

^{208}Pb is the heaviest doubly magic nuclear system studied so far. It is a stable isotope. ^{78}Ni and ^{132}Sn are more difficult to produce and study because of their larger neutron excess. This is illustrated in Figure 1.2. ^{132}Sn has eight neutrons in addition to its heaviest stable isotope ^{124}Sn. The situation is even more difficult for ^{78}Ni, where this number is 14. The neutron-separation energy drops with the neutron excess, and this implies technical difficulties in the production of neutron-rich nuclei. Recently, with the development of radioactive nuclear beams (RNB) it became possible to explore more and more exotic nuclei far from the line of beta stability produced in relativistic heavy ion reactions [6, 7]. The experimental study of isomeric states in the ^{132}Sn region applying RNBs forms the major part of this work. In addition, so-called K-isomers (see Sec. 2.4) have been investigated.

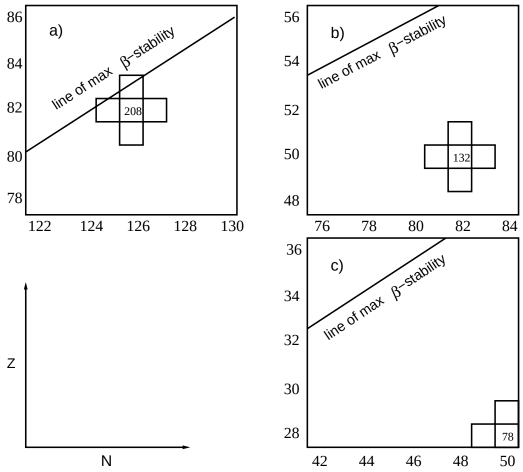

Figure 1.2: Comparison of the location of the three doubly magic nuclei ^{208}Pb (a), ^{132}Sn (b), and ^{78}Ni (c) relative to the line of β-stability. The large neutron excess of ^{132}Sn and ^{78}Ni implies experimental difficulties due to low production cross sections.

Chapter 2

Physics of selected neutron-rich nuclei

2.1 Neutron halos and skins

Let us focus on the very neutron-rich side of the nuclidic chart, which is the subject of the present study. The neutron-drip line is experimentally known only from hydrogen ($Z = 1$) up to oxygen ($Z = 8$). In the neutron-rich isotopes of the light elements the so called halo phenomenon exists. The halo is formed by the loosely bound neutrons surrounding the core. Due to the weak binding nuclear matter is distributed in regions not allowed classically. Thus halo nuclei are characterized by very large radii. Secondly, they are very diffuse and their properties are greatly dominated by surface effects. Halo phenomena are the subject of study of many experimental and theoretical groups.

In the heavier neutron-rich nuclei, the excess of neutrons is expected to form a neutron skin. The chemical potentials of protons and neutrons shift away from each other and the surface region is predominantly occupied by neutrons. Figure 2.1 presents the difference between neutron and proton radii for tin isotopes, calculated in different approaches [2]. The calculations are done in mean-field interactions with relativistic (NL) and non-relativistic Skyrme forces (Sk, SL). The two groups of calculated results predict the evolution of a neutron skin with increasing neutron excess. This is expected as a global trend for very neutron-rich nuclei. The first experimental evidence for such a systematic trend was recently observed for sodium isotopes [8]. The calculations presented in Figure 2.1, however, fall into two different groupings, indicating that our understanding of what happens far from stability is far from complete.

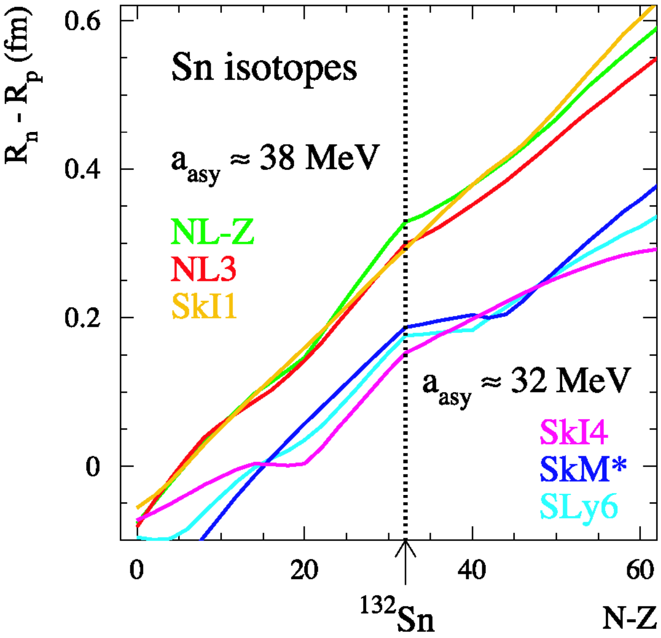

Figure 2.1: Neutron skin thicknesses calculated with relativistic (NL) and non-relativistic (Skyrme forces Sk, SL) mean-field calculations for Sn isotopes. The figure is taken from [2].

2.2 Shell evolution far from stability

The present understanding of nuclear structure in the vicinity of doubly magic nuclei is based on the nuclear shell model. According to this model the nucleons occupy quantized orbits grouped in shells. Measured proton and neutron separation energies give experimental evidence of an enhanced stability of nuclei with certain numbers of neutrons and protons, the magic numbers.

In nuclei with large excess of neutrons, the coupling of bound neutron states with unbound continuum states above the Fermi level is expected to soften (or “quench”) the shell gaps [9]. Mean-field calculations predict that certain neutron shell gaps “melt” with increasing N/Z ratio, and new shell sequences will possibly appear. Figure 2.2 shows the Z dependence of the two-neutron separation energies S_{2n} along the $N=$ 50 and 82 magic numbers [10]. According to the calculations, the shell gap is reduced from 6 MeV for ^{100}Sn to 2 MeV for ^{78}Ni (Fig. 2.2 a). In fact, in this picture ^{78}Ni is not as good magic nucleus as ^{132}Sn and the “meltdown” of magic number 82 for neutrons is predicted to occur at $Z \leq 40$.

The quenching of the neutron shell structure with increasing neutron number is not a generic property of all effective interactions, as discussed in ref. [11]. Calculations

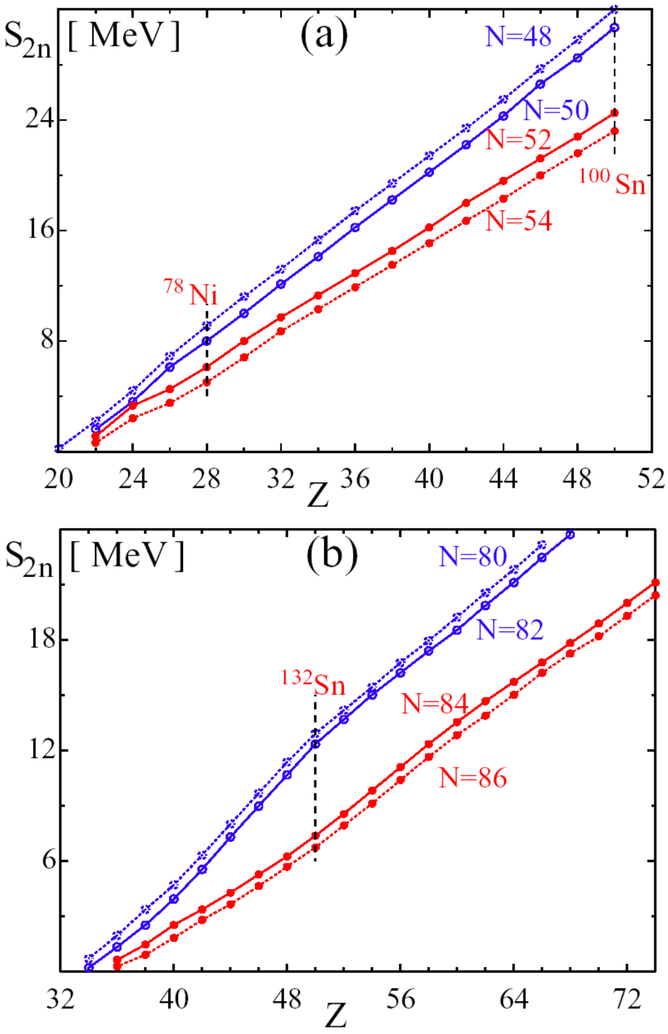

Figure 2.2: Z dependence of the two-neutron separation energies S_{2n} along the $N=$ 50 and 82 magic numbers, calculated in the mean-field approach. The S_{2n} parameter serves as a measure for the shell gap. The figure is taken from [2].

indicate that a new interaction needs to be developed, along the Skyrme approach, to correctly take into account energy densities and to increase the predictive power for more exotic systems. To fine-tune the interaction, experimental data on both global nuclear properties as well as spin-dependent ones are needed for neutron-rich systems.

2.3 Isomers

One way to explore the phenomena described above is to study *isomeric states* in nuclei populated directly in a nuclear reaction. The isomer decay reveals important spectroscopic information for the isomer itself, and for the excited states through which it decays.

An *isomeric state* is a long-lived excited state in a nucleus. Isomeric half-lives may vary from a few nanoseconds to years. There are different reasons for the formation of an isomer. A common requirement is that the properties of the initial excited state should be very different from those of the final state to which the isomeric transition occurs. Often the reason for a delayed transition in nuclei is the small energy difference between the initial and the final state. The long half-life is governed by the decay probability dependence on the transition energy. General formulas can be found in [12]. In the case of an $E2$ transition, for example, the decay probability depends on the energy to the power of five. Other reasons include a large change of the spin to match the state to which the isomer is decaying, or a change in the spin orientation relative to an axis of symmetry, or a change of the shape of the nucleus. These situations depend on the detailed shell structure of the neutron and proton orbitals in each nucleus.

The coupling of valence particles and holes in nuclei near doubly-magic ^{132}Sn often gives rise to isomeric states with moderate spin and with lifetimes in the microsecond regime. In the Hf/W/Os region, a special kind of isomerism occurs, namely the "K-isomerism". The reason for forming such isomers is discussed in Section 2.4.

2.4 K-isomers in the Hf/W/Os region

In the $A \approx 170-190$ rare-earth nuclei a specific type of isomerism occurs, originating from valence particles occupying high-j orbitals with a large projection Ω_j of the angular momentum on the nuclear symmetry axis. These nuclei are axially symmetric. Therefore, the collective rotation R takes place about the short axis, perpendicular to the symmetry axis, and the collective angular momentum is thus zero along the symmetry axis. The coupling of the single-particle angular momenta is shown in Fig. 2.3. The projection of the total angular momentum on the symmetry axis is $I_3 = K+R = K$, where K is built by the single particle momenta Ω_j, $K = \sum_j \Omega_j$, and is a constant of motion (i.e. it is a good quantum number characterizing the system). The decay of such high-K states to low-K rotational states is often hindered due to the large difference, ΔK, between the initial and final states. The only way such high-K states can decay is via large alternation of the orientation of the total angular momentum, which is forbidden via low multipolarity transitions if the K projection is a good quantum number. Thus, such states become long-lived, i.e. isomeric. The hindrance factor grows exponentially with the degree of K-forbiddenness, $\Delta K - \lambda$ [13], where λ is the multipolarity of the transition.

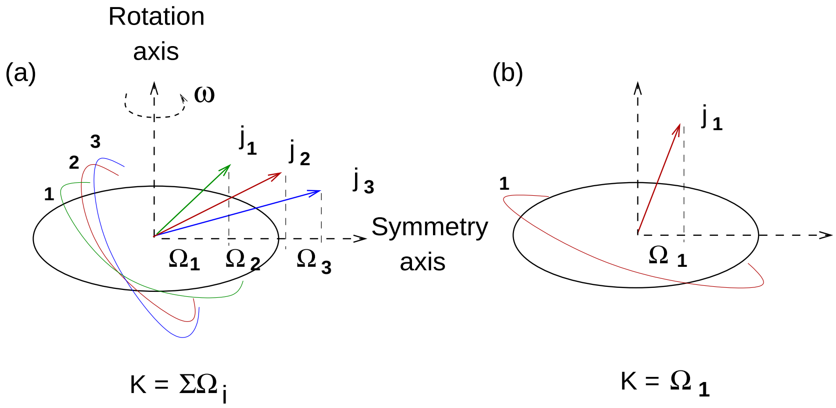

Figure 2.3: K-isomerism is a characteristic feature of deformed nuclei with axial symmetry (a). The collective angular momentum along the symmetry axis is zero, and the projection of the total angular momentum I is built by the sum of the projections of the single particle momenta j_i. Decay to a lower K state (b) requires rearrangement of nucleons and a change in the orientation of the angular momentum relative to the axis of symmetry.

The observation of isomeric decay by K forbidden transitions implies that there must be some mixing of K values, i.e. the states involved are not pure from a quantum mechanical point of view. Suggestions for the mechanism of "K-mixing" include Coriolis mixing, and γ-deformation tunneling [14]. Coriolis mixing arises because a rotating nucleus is not an inertial frame of reference, and the orientation of a nucleon's orbit is modified by the rotation of the nucleus. The γ-tunneling involves shape fluctuations where the deformation of the nucleus changes from prolate shape ($\gamma = -120°$) to prolate shape ($\gamma = 0°$) through the intermediate oblate ($\gamma = -60°$) shape.

K-mixing raises the question of the limits of K-forbiddenness and the limits of the K-isomerism. It has been predicted that this region will extend into the neutron-rich Hf/W/Os region with $A \approx 180 - 200$ [15, 16]. These nuclei are expected to be triaxially deformed (i.e. the size of the nucleus along all three axis is different), and the isomers are expected to have shorter lifetimes.

2.5 The ^{132}Sn region

The properties of the doubly-magic core of ^{132}Sn has been discussed in [17, 18]. The core excitation of ^{132}Sn itself is studied in details and it is well known. The first excited state in ^{132}Sn is at 4.0 MeV, which suggests that the single-particle states in the surrounding nuclei should be rather pure. The simplest excitations in doubly-magic and in the neighboring nuclei are particle-hole (p-h) excitations. The p-h states of these nuclei form level multiplets where the individual states often have a very simple structure with regards to admixture of configurations. The mapping and identification of such multiplets may give immediate information on the nuclear two-body matrix elements and single-particle energies, which are crucial elements in the theoretical models. Almost all single particle (hole) energies in the region have been measured as summarized by Grawe and Lewitowicz [19]. A number of empirical two-particle, two-hole, and particle-hole multiplets have been identified as well. The properties of excited states originating from proton $g_{9/2}$ holes relative to the ^{132}Sn core and the neutron $f_{7/2}$, $h_{9/2}$ and $i_{13/2}$ particles in the Sn isotopes with $N > 82$, will give information on the shell structure in this region. A challenging experiment is the systematic study of the $N = 82$ isotones below $Z = 50$, towards the nuclei for which the shell quenching was predicted. However, the more exotic the system is, the more difficult the experiments become.

Chapter 3

Experimental techniques

3.1 Production mechanisms

Depending on which part of the nuclidic chart and what parameters of the nuclei one wants to study, different production mechanisms can be applied. For the spectroscopy of proton-rich and stable nuclei the most suitable method is a heavy-ion fusion evaporation reaction. In this reaction nuclei are produced in excited states with relatively high angular momenta and excitation energies [20]. In projectile fragmentation the maximum yields and production cross sections are along the β- stability line, but this type of reaction populates also proton-rich as well as neutron-rich nuclei. Nuclear fission is the most suitable method for producing intermediate mass neutron-rich nuclei. This work is focused on γ-ray spectroscopy of isomer decays of neutron-rich nuclei, produced in projectile fragmentation and in-flight fission. The following two sections of the chapter will give more detailed explanation of the two production mechanisms.

3.1.1 Projectile fragmentation

When a heavy projectile, accelerated to energies much above the Coulomb barrier, interacts with a target nucleus, the probability for a fragmentation reaction is very high. Depending on the actual energy of the bombarding ions and on the impact parameter, several different regimes are possible. At low energies ($E/u < 20$ MeV/nucleon) there are several mechanisms contributing to the reaction, including Coulomb scattering, incomplete fusion, and fusion evaporation reaction [21]. Reactions occurring at much higher energies ($E/u > 200$ MeV/nucleon) are considered to be "pure" fragmentation [22]. In this energy regime depending on the impact parameter we can have projectile fragmentation in the case of peripheral collisions, and multifragmentation takes place in the case of central collisions. The "pure" projectile fragmentation is a two step process as discussed in ref. [22].

Figure 3.1 shows a schematic view of the two-step reaction. In the peripheral collisions between the bombarding heavy ion and the target nucleus, the nucleons in the overlapping area ("participants") become very hot and excited nuclear matter, which is almost immediately abraded off. This is a very fast process which occurs within 10^{-21}s. The remaining part of the projectile ("spectator") undergoes statistical evaporation (also known as "ablation") of particles and light clusters, after which we observe the final products of the reaction. This step takes about 10^{-16} s. The momenta (or velocities) of the final products is very similar to those of the projectile. Due to the high energy involved in the collision, a rather extensive range of the mass of the final observed products can be obtained.

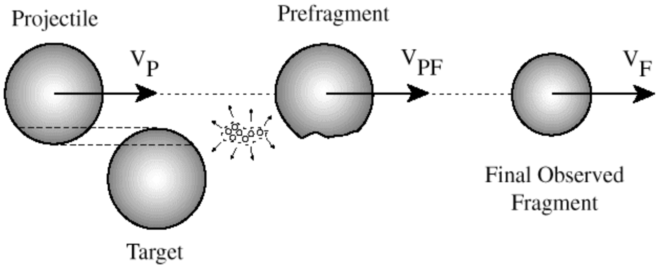

Figure 3.1: Projectile fragmentation at relativistic energies ($E > 200$ MeV/nucleon, $\beta > 0.7$). The final observed fragment has momentum very similar to the one of the projectile. The figure is from Ref. [21].

3.1.2 In-flight fission

The best method to produce (very) neutron-rich intermediate-mass nuclei is nuclear fission. In this work the so-called in-flight or projectile fission of heavy-ions at relativistic energies has been used. In this reaction the heavy ion (for example ^{238}U) is accelerated to relativistic energy. The target nucleus can be light (e.g. ^{9}Be) or heavy (e.g. ^{208}Pb), inducing fission by peripheral nuclear interactions for the U/Be system, or by dissociation in the electro-magnetic field for the U/Pb system [23].

The excited projectile splits into two relatively cold fragments, which are emitted in opposite directions from each other in the reference system of the fissioning nucleus (Figure 3.2). The products are isotropically distributed. In the laboratory frame the distribution transforms into a narrow cone centered in the beam direction. The process is shown schematically in Figure 3.3.

The velocity of the fission fragments in the laboratory frame is the relativistic addition of projectile and fission velocities β_0 and β_F. Thus, the forward flying fragments get an additional 'kick' in momentum. In that sense the projectile fission is an exothermal reaction for the products distributed in the forward semi-sphere with

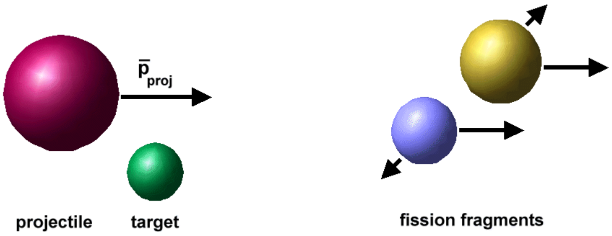

Figure 3.2: Projectile fission at relativistic energies ($E > 500$ MeV/nucleon, $\beta > 0.8$). The two fission fragments are relatively cold, and are emitted in a forward and backward direction in the reference system of the projectile.

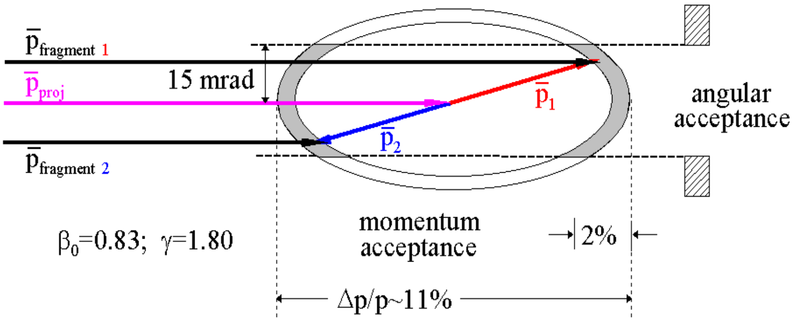

Figure 3.3: Momentum distribution of the relativistic fission fragments in the laboratory system. The part of the distribution accepted by the separator is indicated by the filled areas.

respect to the beam direction. The relativistic character of the process has a great advantage compared to the fission at rest. It allows the use of a spectrometer for the extraction of a secondary beam as explained in section 3.2.1, and identification of the reaction products event-by-event, as discussed in sect. 4.1. In his Ph.D. thesis Engelmann [24] investigates the reaction kinematics and shows that there is a gain factor with respect to the fission at rest: the high velocity of the fissioning projectile nucleus (≈ 83% of the speed of light for a primary beam with $E = 750$ MeV/u) leads to an optimal transmission for those fragments, flying in either forward or backward direction with respect to the beam. This means that for equal fission rates one can observe nuclei produced with cross sections up to three orders of magnitude smaller than the one we can observe with fission at rest.

Due to the limited acceptance of the FRS spectrometer (Section 3.2.1), not all reaction products can be transmitted and studied simultaneously. The opening angle of the cone is about ±30 mrad, and the angular acceptance of the spectrometer is ±15 mrad.

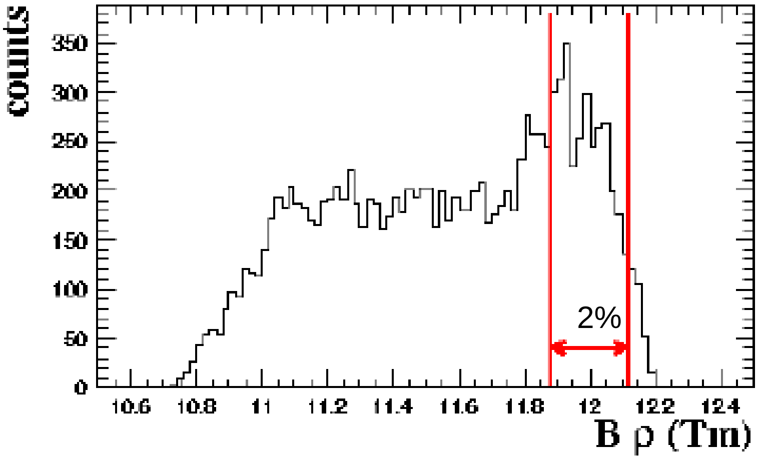

Figure 3.4: MOCADI simulation of the distribution of ^{130}Sn fragments after fission of ^{238}U at 750 MeV/nucleon. The rectangular window represents the acceptance of the FRS.

Figure 3.4 presents a MOCADI simulation (see Section 3.2.2) of the kinematic properties of ^{130}Sn ions produced in ^{238}U fission at 750 MeV/nucleon. The magnetic rigidity $B\rho$ of the fragments is proportional to their longitudinal momenta. The 2% momentum acceptance of the FRS is indicated. This figure helps to understand the difficulty in selecting fission fragments with the FRS, not only because of the limited acceptance but also because of the shape of the distribution. There have been long discussions within the FRS community, and different opinions on how to select in the most efficient way the part of the distribution resulting in the highest rate for the neutron-rich isotopes of a given element. Is there a dependence of A/Z (or on how many neutrons that were evaporated) on the velocity/momentum? To try to answer that question we have measured the dependence of the production/observation rate on the momentum of the fission products. The results are summarized in Chapter 5.

Figure 3.5 illustrates how the scan in the momentum distribution of the fission fragments was done. It can be done either by tuning the FRS to shift the selection window, or by keeping the FRS settings and changing the energy of the primary beam, as shown in the figure.

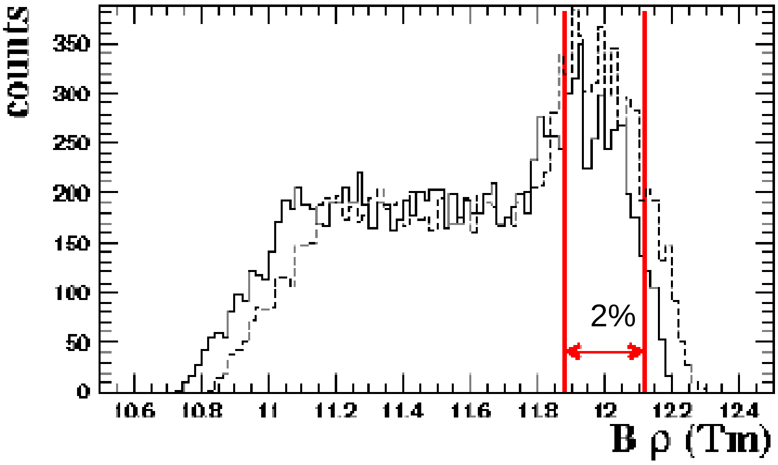

Figure 3.5: MOCADI simulation of the distribution of ^{130}Sn fragments after fission of ^{238}U at 750 MeV/nucleon (solid), and 759 MeV/nucleon (dashed). The rectangular window represents the acceptance of the FRS. By changing the primary beam energy in steps, a scan of the momentum distribution of the fission fragments is achieved.

3.2 The FRagment Separator

3.2.1 Separation of the reaction products

In both production mechanisms described above up to 10^3 reaction product species can be created in the target due to the high energy involved in the reaction. To separate only the ions which we are interested in, i.e. to obtain a pure secondary radioactive beam, we use a tool called the FRagment Separator (FRS). It is an achromatic magnetic forward spectrometer [25]. Heavy-ion beams with magnetic rigidities from 5 to 18 Tm can be analyzed by the device. Figure 3.6 shows the main parts of the FRS. There are four 30° dipole magnets determining four independent stages of the spectrometer and a number of quadrupole and sextupole magnets providing variable magnetic fields up to 1.6 Tesla. The quadrupole magnets before each dipole are designed to achieve a high resolving power by properly illuminating the field volume of the bending magnets. The ion-optical conditions at the four focal planes S1 to S4 are determined by the quadrupoles following each dipole. The function of the sextupole magnets placed in front of and behind each dipole is to provide correction for second-order abberations.

A secondary-electron transmission detector (SEETRAM) placed upstream of the target position measures the beam intensities [27]. In the target area and at each focal plane, two-dimensional grids with gas amplification and current readout are used for beam alignment and count rate measurements. Heavy-metal alloy slits can be used to mechanically reduce the beam count rate if it is necessary, or to prevent the penetration of the primary beam through the separator.

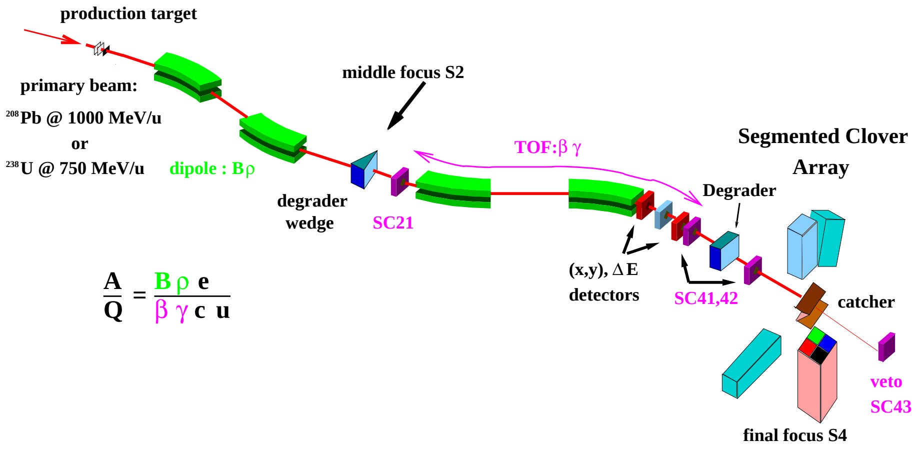

Figure 3.6: Schematic view of the FRagment Separator at GSI. After production in a target, the ions of interest are selected and separated with the help of the spectrometer. The total flight path is 76 m. After passing various detector and degrader systems the selected products are brought to the final focal plane where delayed γ-ray spectroscopy can be performed. The figure is from Ref. [26]

The separation is based on magnetic analysis combined with energy losses in matter ($B\rho - \Delta E - B\rho$ method [28]). The reaction takes place in the target, and the ions are selected by their mass to charge ratio A/q in the first stage of the separator. In this first step, up to about 10^2 different reaction products are selected. Energy degraders with variable thicknesses are placed at the different focal planes of the separator. To introduce different energy loss for the fragments with different momenta a special wedge-shaped degrader is placed at the central focal plane S2. The different atomic energy loss of the ions penetrating the degrader provides an additional selection criterion. The best spatial separation can be obtained with a degrader shape which preserves the achromatism of the spectrometer. In this way at the final focal plane S4 we obtain a purified secondary beam consisting of the ion for which the separator was tuned and 10-15 neighboring isotopes. This will be called the "production setting" and the fragment for which the separator has been tuned is referred to as the "setting fragment".

The particle trajectory detection is performed by using multi-wire proportional chambers [29] installed at all of the focal planes. At the middle (S2) and final (S4) focal planes, pairs of these detectors are used for particle tracking to analyze the primary beam or secondary radioactive beam with respect to position, angle, and $B\rho$ value. The energy loss ΔE is measured in a MUltiple-Sampling Ionization Chamber (MUSIC) [30].

Secondary beams prepared by the FRS can be transferred to other experimental areas for performing different measurements, such as the experimental storage ring (ESR) where masses can be measured [31], or to the ALADIN/LAND setup for secondary reaction experiments [32].

3.2.2 Transmission simulations

The Monte Carlo code MOCADI [33] can be used to simulate the transmission of reaction products through the FRS. The code not only takes ion optics into account, but also is designed to realistically include atomic and nuclear interaction processes such as scattering and secondary reactions.

In order to plan the stopping of the secondary beam the energy losses in matter (degraders, detectors, air) are calculated with the code ATIMA. The physical processes implemented in the program are discussed in Ref. [34].

Figure 3.7: Photo of the final focal plane of the separator. The aluminum Z-shaped catcher of thickness 4-6 mm is surrounded by Ge clover detectors.

3.2.3 Fine-tuning of the FRS ion optics

In the start-up phase of each FRS experiment the ion optics of the separator has to be fine-tuned in order to create a reference magnet setting. This is done with a low intensity primary beam, the magnetic rigidity of which, $(B\rho)_{primary}$, is known at the entrance of the FRS. The beam has to be aligned onto the target position, meaning that it has to be centered and perpendicular to the target surface. This is monitored by a system of position sensitive current grids. After the beam is aligned onto the target position, the current grids are removed and the FRS magnets are set to the primary beam rigidity. The beam is transmitted through the FRS, and at each focal plane its position is measured with multi-wire detectors. The dipoles are fine tuned so that the beam is centered at the focal planes. The magnetic field is measured by Hall probes and for each dipole the effective radius ρ_{dipole} is determined:

$$B_{Hallprobe} * \rho_{dipole} = (B\rho)_{primary} \tag{3.1.1}$$

Thus a reference magnetic setting is created and saved. It is the starting point for all other settings. During this procedure, however, all materials are removed from the beam axis (except for the detectors monitoring the alignment) to avoid complications due to changing of the primary beam rigidity. Therefore, the effective thicknesses of layers of matter which will be used in the production setting (production targets, plastic scintillator SC21, and S2 degraders), have be to measured. This is done by calculating with ATIMA the expected primary beam rigidity before and after the layer of matter, setting the FRS correspondingly, inserting the matter and measuring the position of the beam after at least one dipole with multi-wire detectors. If the beam is not centered downstream of the layer, the FRS is adjusted to center the beam. From the difference between the measured $B\rho$'s before and after the layer, the energy loss in the matter is calculated. The thickness to which the energy loss corresponds is calculated with ATIMA.

3.2.4 Calibration of the particle identification detectors

In order to calibrate the detectors involved in the identification procedure a set of measurements with the primary beam through the separator at low intensity and with different, well defined energies is done before each production run. The time-of-flight (TOF) calibration is based on a linear dependence of TOF*β, which equals the flight path, on the velocity of the fragment, β. During the calibration procedure, measurements are performed for several well defined reference beam velocities, which should cover the expected velocities of fragments in the production run. In the cource of this measurements a calibration of the MUSIC detector is achieved as well. The coefficients in the quadratic relation between the energy loss measured by the detector ΔE and the fragment charge Z, as well as the detector responce to different velocities are then empiricaly determined in the calibration. On Figure 3.8, the TOF and MUSIC calibration curves from Experiment IV (see Table 3.1) are plotted.

3.3 γ-ray detection

For the purpose of isomer γ-ray spectroscopy the beam is stopped at the final focal plane of the spectrometer and the products of interest are implanted in a catcher foil made of aluminum or plastic (Fig. 3.6 and Fig. 3.7). In all experiments on which this

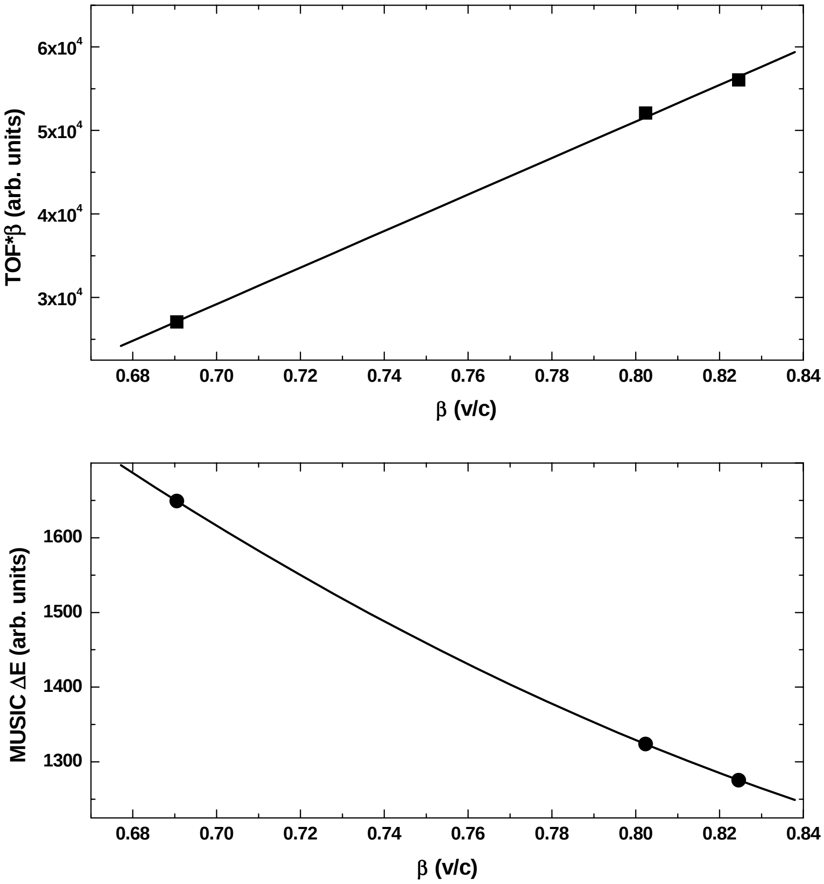

Figure 3.8: TOF and MUSIC calibration measured during Experiment IV. The relation between the flight path (TOF*β) and the velocity, β, is expected to be linear. The response of the MUSIC detector ΔE, however, has a quadratic dependence on β.

work is based (see Table 3.1), the catcher was surrounded by segmented germanium detectors of clover type [35], in which delayed γ-rays emitted by the implanted ions were detected. γ-rays from the decay of any isomeric state were recorded within a 80 μs time gate, which was started with the detection of a heavy ion. The flight path of the ions trough the separator is about 300 to 400 ns, which typically sets a lower limit of about 100 ns for the lifetimes which can be studied, but exceptions have been observed (Section 5.1). By using a combination of TDCs (time-to-digital-converter) and TACs (time-to-analog-converter), the timing information from the γ-rays could be recorded in 0 to 8 μs and 0 to 80 μs ranges. The germanium detectors were energy calibrated with standard sources. A time calibration was performed using a time calibrator.

3.3.1 Detector systems

A summary of the different experiments is given in Sect. 3.4. In Experiments I and II the ions of interest were implanted in an aluminum catcher, whereas a plastic catcher was used in Experiments III and IV. In Experiment I the catcher was surrounded by three segmented clover germanium detectors from the EXOGAM collaboration [35] and a large-volume GSI 'VEGA' (Versatile and Efficient GAmma-Detectors [36]) detector. Each detector consisted of four separate germanium crystals. Four EXOGAM clover detectors and one VEGA detector were used in Experiment II. The VEGA was mounted below the catcher, two EXOGAM detectors were placed to the sides and two above the catcher. Two VEGA detectors were used in Experiment III, one mounted above and one below the catcher. Two VEGA and four EXOGAM detectors were mounted in Experiment IV. The VEGA detectors were placed above and below the catcher, and the two EXOGAM detectors on each side of it.

3.3.2 Efficiency calibration

To determine the efficiency for detecting γ-rays, an absolute efficiency calibration of the Ge detector set-up is needed. Because of the large size of the beam spot and the varying implantation depth, it is important to take into account the geometry of the Ge detector set-up and possible absorption in the catcher material. Therefore calibration spectra were recorded using a standard source with known activity placed at several positions along the x-direction of the catcher, and on both sides of the catcher (upstream and downstream). One approach is to consider the efficiency for each individual detector crystal, as was done in Experiment I. Alternatively, the efficiency for the complete set-up may be considered, as in the case of Experiments III and IV. The calibration curves for 3 geometrical points measured during experiment IV are presented in Fig.3.9. From the figure one can note that except for energies below 100 keV, all curves cluster together within $\pm 10\%$ of each other. As this variation is considered to be small in comparison to other sources of uncertainty, average efficiency curves were used in the evaluation of Experiments III and IV. In the case of Experiment II no absolute efficiency calibration was performed.

3.4 Summary of performed experiments

The thesis is based on four experiments performed at the FRagment Separator (FRS) at GSI, Darmstadt, using the techniques described above. Table 3.1 summarizes some technical details about the experiments. In April 1999 we used projectile-fragmentation of ^{208}Pb at 1 GeV/nucleon to produce neutron-rich nuclei in the Hf/W/Os region to study K-isomers (Experiment I). In Experiments II, III and IV, performed in December 1999, December 2001 and July - August 2002 we studied neutron-rich nuclei in the ^{132}Sn region produced in projectile-fission of ^{238}U at different energies (see Table 3.1).

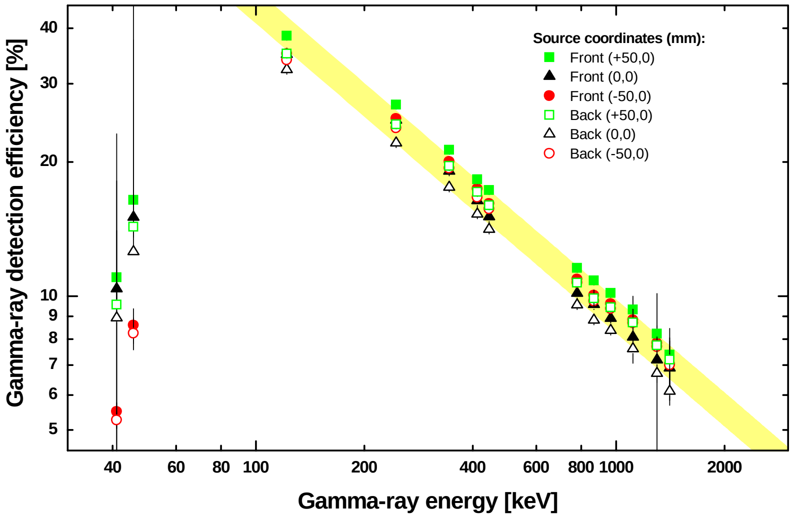

Figure 3.9: Calibration curves measured during experiment IV. The solid (open) symbols represent data measured with Eu source placed at the front (back) side of the catcher. The curves are fitted above 100 keV with an exponent.

Table 3.1: Technical data about the experiments

Experiment	Beam	Energy, MeV/nucleon	Target	Purpose
I	^{208}Pb	1000	1.6 g/cm^2 ^{9}Be	isomer search in n-rich Hf/Os/W
II	^{238}U	750	1.0 g/cm^2 ^{9}Be	isomer search in the vicinity of ^{132}Sn
III.a	^{238}U	750	1.0 g/cm^2 ^{9}Be	isomer search in the vicinity of ^{132}Sn
III.b		750-759	1.0 g/cm^2 ^{9}Be	momentum distribution scan
III.c		732	1.0 g/cm^2 ^{208}Pb	isomer search in the vicinity of ^{132}Sn
IV	^{238}U	732	1.0 g/cm^2 ^{208}Pb	isomer search in the vicinity of ^{132}Sn

In Experiment III data with two different targets were collected, namely with a 1 g/cm^2 ^{9}Be target (Experiment III.a) and a 1 g/cm^2 ^{208}Pb target (Experiment III.c). The purpose of using two different targets was to compare the population of high spin states in the fission reaction with a target as light as Z=4 and as heavy as Z=82. This was done by measuring the isomeric ratios in a number of known isomers with both targets (see Section 4.4). Additional information was achieved by the measured production rates with the two targets.

Experiment III.b scanned the momentum distribution of the fission fragments (Section 3.1.2). This experiment was done with a ^{9}Be target. Isomeric ratios and production rates were measured and compared for the different groups of fragments.

Chapter 4

Analysis

4.1 Identification of the reaction products

As pointed out previously, several thousand different reaction products may be produced in relativistic fission or fragmentation of a heavy projectile. The FRS is typically operated so as to reduce the number of different fragment species that reach the final focus to about 10-20. Nevertheless the ions that are transmitted need to be identified on an event-by-event basis. The identification is (mainly) done in the second stage of the separator. It is based on measurements of time-of-flight and energy loss, combined with information from position-sensitive detectors and the magnetic fields of the separator dipole magnets.

The time-of-flight (TOF) of the fragments is measured as the time difference between the plastic scintillators SC21 and SC41, placed at the middle focal plane after the S2 degrader, and at the final focal plane S4 after the vacuum window of the last magnet (cf. Figure 3.6). The velocity v of each ion is calculated from the TOF and the flight path. Position determination is very important not only for the purpose of using the spatial separation of the ions, but to achieve the proper geometrical corrections to the TOF - respectively velocity, and to the magnetic rigidity of the second stage, $B\rho_2$. The $B\rho_2$ value can be calculated from the expression:

$$B\rho_2 = B\rho_0(1 - \tfrac{x_4 - V_2 x_2}{D_2}) \ , \tag{4.1.1}$$

where $B\rho_0$ is the magnetic rigidity of particles at the ion-optical axis. ρ_2 is the effective radius of the fragments in the second stage of the separator. V_2 and D_2 are properties of the ion optics of the FRS second stage, namely magnification and dispersion. x_2 and x_4 are the positions of the ion in the x-direction at the intermediate and the final focal planes, respectively.

The position determination at S4 is done with the multi-wire proportional counters, but the scintillators can be used for position measurements in the horizontal direction as well. The position information from the scintillators is obtained from the time difference between signals from the left and right readout of the detector.

Combining the velocity and $B\rho_2$ information, one can define the mass-to-charge ratio A/q for each fragment via the expression:

$$A/q = \frac{e}{uc}\frac{B\rho_2}{\beta\gamma} , \tag{4.1.2}$$

where e is the elementary charge, u is the atomic mass unit, $\beta = v/c$ is the ratio of the velocity of the ion to the speed of light, and γ is the Lorentz factor ($\gamma = 1/\sqrt{1-\beta^2}$). The proton number Z of each ion can be estimated under the assumption:

$$\Delta E = Z^2 f(\beta), \tag{4.1.3}$$

where the energy loss ΔE is measured in a MUltiple-Sampling Ionization Chamber (MUSIC). The function f, which depends on the ion velocity [37], is deduced from the primary beam calibration measurements, which are described in Section 3.2.4. Figure 4.1 shows the ΔE spectrum measured for the ^{131}Sn production setting from Experiment II. When analyzing only the fully stripped ions the following relation is valid:

$$A/q = A/Z, \tag{4.1.4}$$

By using these relationships, unambiguous particle identification in terms of A, Z, and position is achieved on an event-by-event basis for each ion. In Figures 4.2 and 4.3 examples of identification maps are given.

4.2 Transmission and losses

There are several factors which affect the transmission of the reaction products through the separator. First of all, one should distinguish the term *optical transmission, T_{opt}*, from the *total transmission, T_{tot}*. The first is a measure of the efficiency of the ion-optics to transmit and focus the beam without losing particles in the process. The total transmission includes additional processes such as nuclear absorption, changes of charge states, and secondary reactions. The total transmission through the separator is typically $\approx$ 50% for fragmentation and $\approx$ 2% for fission products. The second process has a much lower transmission due to the specific kinematics of the in-flight fission reaction (Chapter 3.1.2).

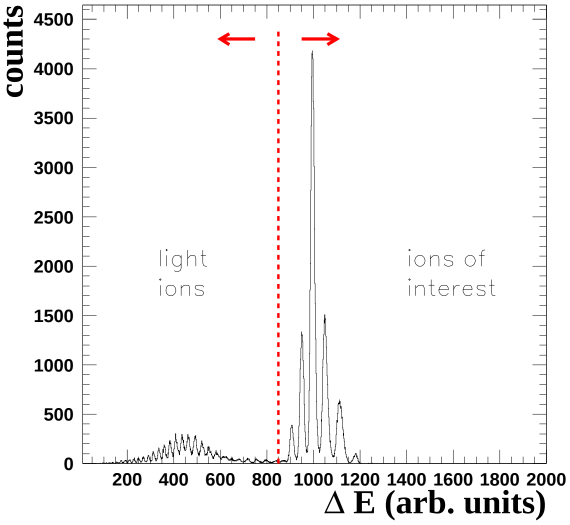

Figure 4.1: Energy loss measurement in the MUSIC detector for all fragments reaching the final focal plane of the separator in the ^{134}Sn setting (Experiment II). A small fraction of light fission fragments is also being transmitted but later excluded in the analysis.

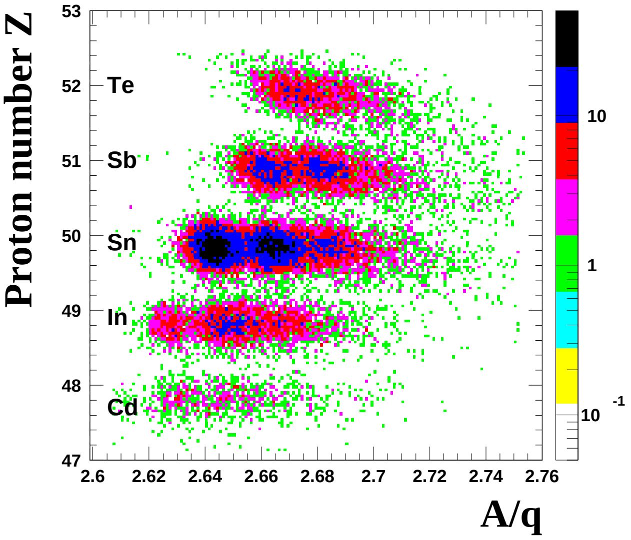

Figure 4.2: Identification plot from the ^{134}Sn setting in Experiment II. The proton number Z is plotted versus the mass-to-charge ratio A/q for fragments reaching the final focal plane of the separator during the setting for ^{134}Sn. Each group represents a different isotope. For each Z several isotopes can be identified.

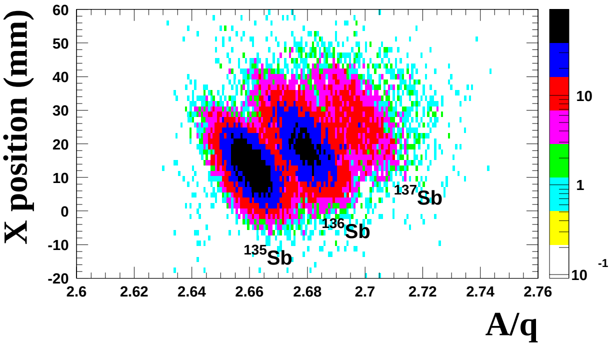

Figure 4.3: Events from the same setting as in Fig. 4.2 with Z selection, presented in different coordinates. The X position of the fragments at the final focus is plotted versus the mass to charge ratio A/q. The Z=50 group is selected and better mass separation is achieved.

When passing different materials or already in the target, some products may pick up or lose electrons and thus change their charge state q. Thus we can transmit simultaneously fully stripped, H-like, and He-like charge states of the ions (H-like implies the presence of one bound electron, etc.). This could lead to misidentification, and is especially important for heavy fragments ($Z > 50$), as in the case of the K-isomer study. However, there are methods to solve this problem. To reduce the number of the fragments which change q by picking up an electron, a niobium stripping foil can be placed after the target, and after each degrader. Ions, which have nevertheless changed their charge state, cannot be spatially separated from the ones which have kept their charge state, but can be separated in the A/q versus S2 x-position space in the second stage of the spectrometer.

In Figure 4.4 the separation of the different groups is illustrated. Three groups of ions can be clearly seen in (a) - those which have not changed their charge state ($\Delta q = 0$), those which have changed it with one unit ($\Delta q = 1$), and with two units ($\Delta q = 2$). The first group predominantly corresponds to fully stripped ions, to some extent contaminated by some H-like ions and with negligible contribution from He-like ions. The second group consists mainly of ions which have picked up an electron at the intermediate focus. In Figure 4.4 panel (b) can be seen that this problem was negligible for products with lower Z. Indeed, 99% of the Sn ions were fully stripped from production to the final vacuum window of the spectrometer. The program GLOBAL [38], developed at GSI, can be used to estimate the overall charge state distributions of the primary and secondary beams. Its capability to simulate the real processes has been tested and excellent agreement between the calculated and measured values has been found.

Additional losses in transmission are caused by secondary reactions of the fragments during their passage through layers of matter. The losses in the S4 degrader can lower the quality of the identification, since it is situated in between the identification set-up and the catcher. Therefore, there is a danger that fragments which have been identified as 'good heavy ions' are destroyed before being implanted (which could lead

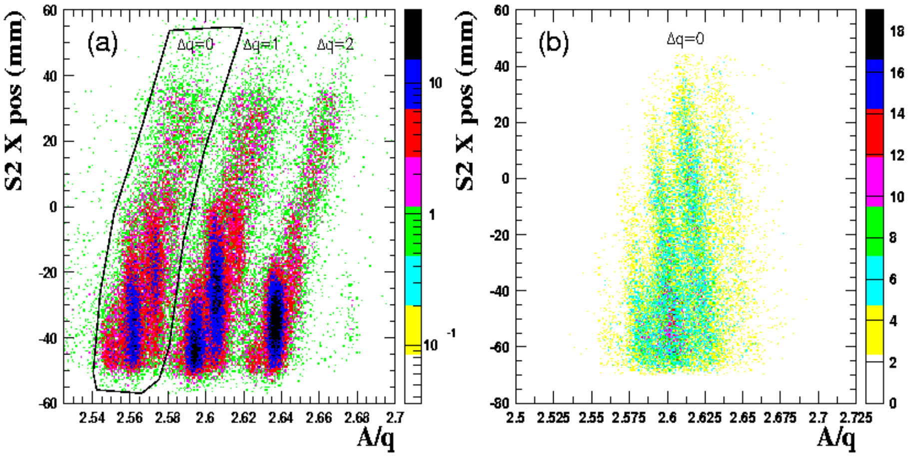

Figure 4.4: The x position at the central focal plane of the separator for all ions that reached the final focal plane. The events which have changed their charge state can be separated in the A/q space. Plot (a) is from the ${}^{191}_{74}$W production setting in the ^{208}Pb fragmentation run, and plot (b) represents all fragments from the ${}^{131}_{50}$Sn setting during Experiment II.

to misassignment of any delayed γ-rays recorded in coincidence). To minimize this problem we used a pair of plastic scintillators placed before and after the S4 degrader to compare the energy deposited by the fragments in the detectors before and after passing the degrader, and suppress 'bad' events (up to 30% for a given isotope). This is illustrated in Figure 4.5.

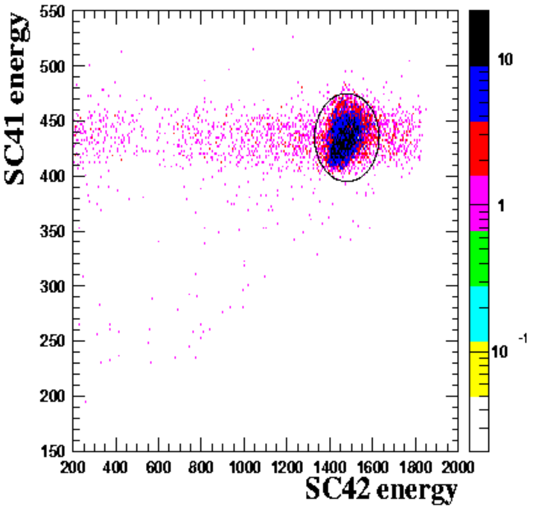

Figure 4.5: Energy loss in the SC41 and SC42 scintillator detectors (cf. Fig. 3.6) in arbitrary units. Only ^{136}Sb ions are selected. The group indicated by the ellipse represents ions which have not changed their proton number in the S4 degrader.

4.3 Delayed γ-ray spectroscopy

A significant aspect of all decay experiments at in-flight separator facilities is the slowing down and subsequent stopping of the secondary beam. This problem is currently being discussed in connection with the new projects taking place at the GSI facility - e.g. the “Stopped Beam” part of the RISING project [39].

The velocity of the products after the target is $\approx 80\%$ of the speed of light. In the second stage of the FRS after the S2 degrader v/c is still ≈ 0.75. In order to implant the products of interest in the catcher we use an adjustable degrader, typically 5-7 g/cm^2 aluminum, at the S4 final focal plane for slowing down the ions. The interactions of the heavy ions with the degrader material cause a prompt burst of X-rays and low energy bremsstrahlung that are emitted during the passage of the heavy ion. The “prompt” burst is significant (see Fig. 4.11) and extends typically to about 250 nanoseconds. It causes a reduction of the effective γ-ray detection efficiency, which is investigated and discussed in Paper V and in Section 4.4.

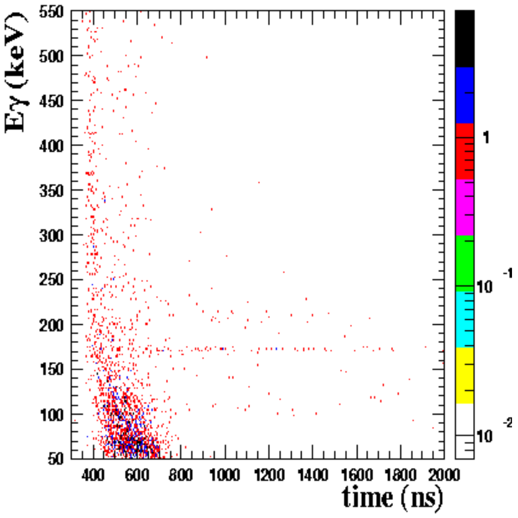

Figure 4.6: Energy-time matrix from one of the Clover detectors gated by ^{136}Sb ions identified in the FRS. The delayed pattern of the 173 keV isomeric transition is clearly seen.

A big advantage of the method is the tagging of γ-rays with a specific ion, which strongly reduces the background and makes possible studies of very weak channels ($<$ 100 ions per day). If one plots the matrix of the energy of the detected γ-rays from a particular isotope versus the time delay between the implantation and γ-ray detection (Fig. 4.6), one can clearly see the decay pattern of the isomeric transition. The advantage of *isomer spectroscopy* is thus that the spectra can be “cleaned” by requiring the detection of delayed γ-rays associated with a given heavy ion. This is illustrated in Figure 4.7.

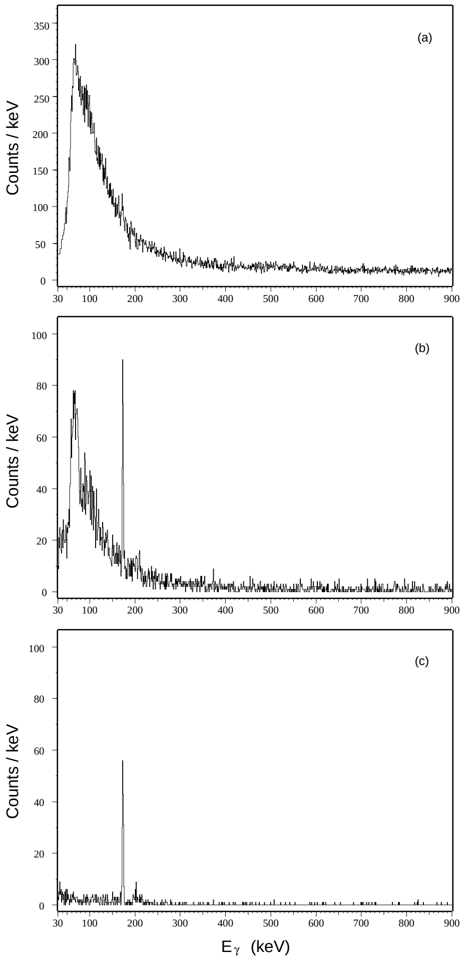

Figure 4.7: Gamma-ray spectra recorded during the ^{134}Sn production run from Experiment II. All gamma events collected in a single Ge crystal are plotted in (a). The background is strongly reduced in (b) by tagging on a selected heavy ion – ^{136}Sb in this case. The prompt burst of low energy bremsstrahlung and X-rays is suppressed (c) by requiring events in delayed coincidence with the heavy-ion. In spectra (b) and (c) a sum of the data from 16 Ge crystals is presented.

If one makes a cut on the energy axis in the time-energy matrix (cf. Fig. 4.6) around a given peak and projects the selection on the time axis, a time distribution related with this transition is obtained. This distribution contains the background as well. The contribution from the background can be determined by gating in the way described above on either or both sides of the γ-peak, projecting on the time axis, and normalizing to the number of channels in the peak gate (Fig. 4.8). For some lower-energy, low statistics isomeric transitions it is difficult to extract a good background distribution in this way due to the prompt burst. For those cases a background distribution has been obtained by gating on wider area on the high energy side close to the peak and normalizing to the prompt part of the spectrum of the non-background subtracted isomer events.

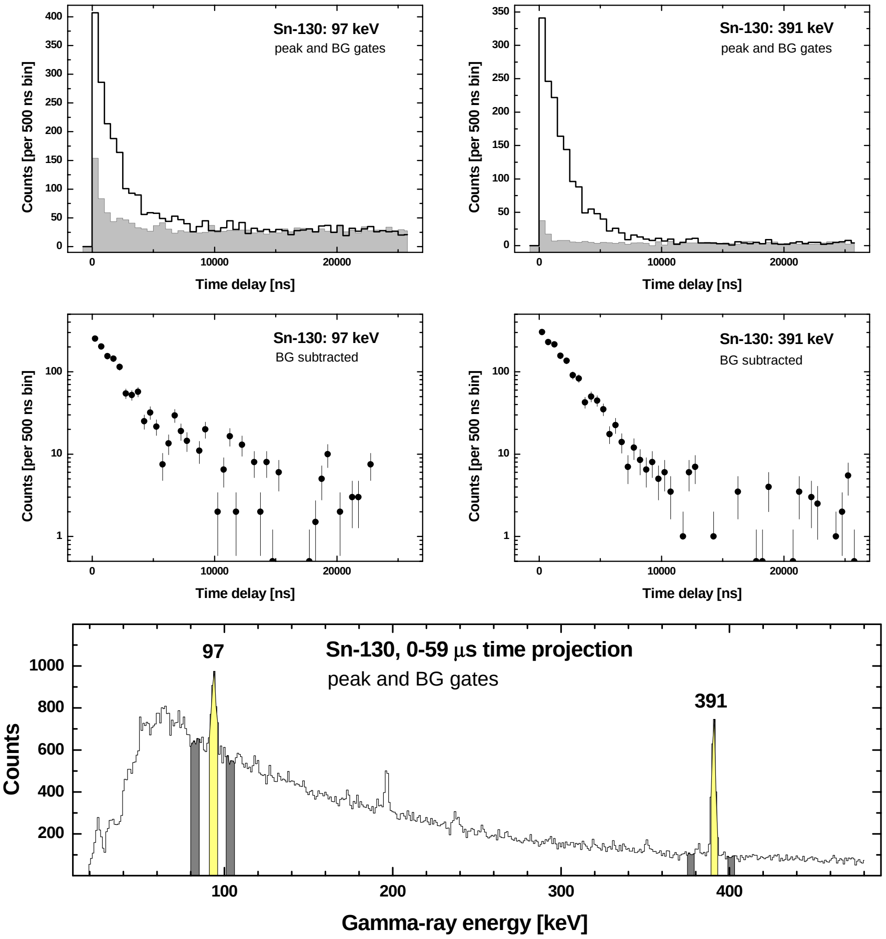

Figure 4.8: Time distribution curves of the 97 keV and 391 keV gamma-lines below the known $I^{\pi} = 10^{+}$ isomer in ^{130}Sn. In the uppermost panels the non-background subtracted time distributions of the two gamma-rays are plotted. The background distributions are shown by the grey areas. The background subtracted data are presented in the two middle panels. The background is determined by gating on both sides of the peak as shown in the lowermost panel.

By fitting the background subtracted time distribution of a given transition the half-life of the corresponding isomeric level can be determined. According to a criterion in Ref. [40], page 252, if the slope of the measured time spectrum is 1.5-2.0 times the prompt slope, then simple slope fitting gives an accurate result. In Figure 4.9 two examples where a slope fit has been applied are presented. For some cases where the

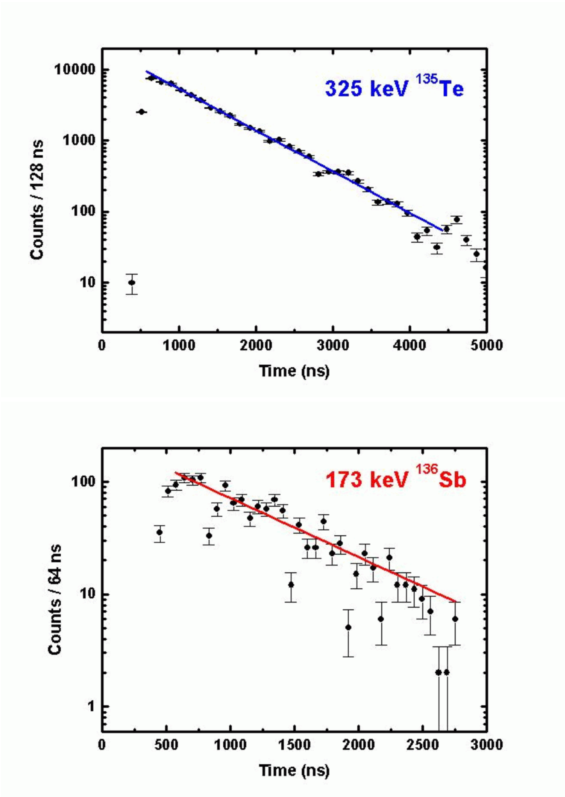

Figure 4.9: Time distribution curves of the (a) 325 keV line from the decay of the well-known $I^\pi = 19/2^-$ isomer in ^{135}Te, and (b) the 173 keV line identified in ^{136}Sb. Background distributions extracted by gating on both sides of the γ-peaks have been subtracted.

available statistics is very low, however, the slope fit is no longer appropriate, and other techniques, such as the maximum likelihood method, should be applied. For a detailed description of such cases see Ref. [66].

4.4 Isomeric ratios

The *isomeric ratio* R is by definition the ratio of the number of ions which have been produced in an isomeric state, and the total number of ions created in the reaction per given species. It is the probability that in the reaction a nucleus is produced in an isomeric state. The population probability of (μs) isomers in either projectile fragmentation or in-flight fission is of great importance from a reaction mechanism study point of view. The knowledge of this ratio and its dependence on the spin and excitation energy of the isomer, will make planning of future experiments more expedient and realistic. The ratio R is defined in the following way:

$$R = \frac{N^{isom}(t{=}0)}{N^{tot}(t{=}0)} \ , \tag{4.5.1}$$

The determination of $N^{isom}(t = 0)$ and $N^{tot}(t = 0)$ is complicated. The schematic plot in Fig. 4.10 helps to understand the determination procedure.

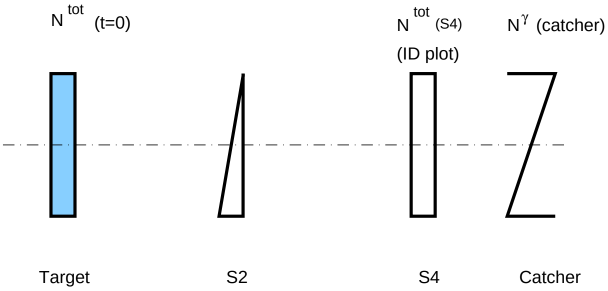

Figure 4.10: Schematic plot of the FRS.

The total number of nuclei of a given species produced in the reaction, $N^{tot}(t = 0)$, and the number of nuclei produced in an isomeric state, $N^{isom}(t = 0)$, can be determined from the experimental data measured at the final focal plane S4, if we take into account the transmission T from the target to S4.

$$N^{tot}(S4) = N^{tot}(t = 0)T_{(target-S4)} \ , \tag{4.5.2}$$

$$N^{isom}(S4) = N^{isom}(t = 0)T_{(target-S4)}F \ , \tag{4.5.3}$$

where F takes into account the in-flight decay. This factor will be discussed in more detail below.

From (4.5.1), (4.5.2) and (4.5.3) we determine

$$R = \frac{N^{isom}(S4)}{T_{(target-S4)}F}\frac{T_{(target-S4)}}{N^{tot}(S4)} = \frac{N^{isom}(S4)}{FN^{tot}(S4)} \ , \tag{4.5.4}$$

The ions in an isomeric state can be determined from the number of detected γ-rays N^{γ} at the catcher

$$N^{isom}(S4) = \frac{N^{\gamma}(catcher)(1+\alpha_{tot})}{G\varepsilon_{\gamma}b_{\gamma}P_{\gamma}} \ , \tag{4.5.5}$$

where α_{tot} is the total conversion coefficient for the isomeric transition, ε_γ is the absolute efficiency for detecting γ-rays of energy E_γ, P_γ is the correction factor for effective efficiency, which takes into account the blocking of the detectors during the low energy prompt flash (see Paper V for details), and b_γ is the branching ratio for γ transitions. G is a correction for the finite time window selected in the analysis procedure when extracting a delayed γ-ray spectrum for the given isomeric transition.

The correction factor G is calculated from:

$$G = exp[-\tfrac{ln2\, t_0}{T_{1/2}}][1 - exp[-\tfrac{ln2\, \Delta t}{T_{1/2}}]] \quad , \tag{4.5.6}$$

where t_0 and Δt are the start of the γ-ray detection and the time window in which data were collected, respectively.

The branching ratios for all transitions following the isomer decay are taken from the literature. The total conversion coefficient α_{tot} for each transition was calculated using a formula developed by the International Network of Nuclear Structure and Decay Data Evaluators [42]. For the new isomers, where no decay scheme has yet been established, assumptions must be made about the branching ratios and multipolarities and only limits can be given for the isomeric ratio.

The absolute efficiency ε_γ is determined from a careful calibration as discussed in Section 3.3.2. As pointed out in Section 4.3, the effective γ-detection efficiency is reduced due to the prompt burst of X-rays and low energy bremsstrahlung coming together with the heavy ion. The data acquisition system allowed the recording of only the first gamma ray in every channel in an event, which led to a high probability for the Ge-crystals to be blocked by the prompt burst. In Figure 4.11 a total germanium time projection gated by a single isotope (^{129}Sn in this case) recorded with a TDC is presented. Three groups of events can be distinguished in such a spectrum - a strong peak corresponding to the prompt burst, followed by delayed events, and events which are outside the range of the TDC. The blocking factor P_γ can be measured by the ratio between the delayed events in such a spectrum and the sum of all events (delayed and prompt) in the same spectrum.

The total number of ions at S4, $N^{tot}(S4)$, we determine from the identification (ID) plot. This number, however, is a projection of the information given by the detectors involved in the particle identification, situated not at the catcher but along the beam axis before the S4 degrader. This implies that the losses in this degrader must be taken in account as discussed in Section 4.2. Thus

$$N^{tot}(S4) = N^{tot}(ID) T_{(S4-catcher)} \tag{4.5.7}$$

The transmission $T_{(S4-catcher)}$ was estimated using the MOCADI code [33].

Combining (4.5.4), (4.5.5) and (4.5.7) we obtain for the isomeric ratio R:

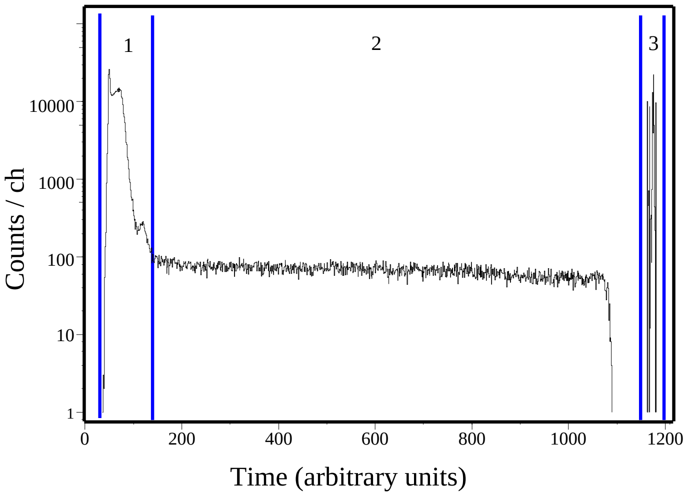

Figure 4.11: Total time spectrum gated on ^{129}Sn recorded with a TDC. Group 1 represents events considered to be prompt, group 2 represents delayed events detected in the Ge detectors and group 3 consists of events which are outside the range of the TDC.

$$R = \frac{N^{\gamma}(catcher)(1+\alpha_{tot})}{FG\varepsilon_{\gamma}b_{\gamma}P_{\gamma}N^{tot}(ID)T_{(S4-catcher)}} \tag{4.5.8}$$

To take into account the in-flight decay one must know the charge state of the ions in the different stages of the FRS, and how this effects the isomeric half-life. For example, if electron conversion is the predominant decay mode of an isomeric state, then the lifetime of this level will be much longer if the atomic nucleus is stripped of all its electrons than in the case of a neutral atom. The factor F is calculated from

$$F = exp[-\sum_i(\frac{ln2\,(TOF)_i}{\gamma_i T_{1/2}^{q_i}})] \quad , \tag{4.5.9}$$

where i are the different stages of the FRS. TOF_i and γ_i, the Lorentz factor, are calculated with the MOCADI code. The half-lives of the ion in the corresponding charge state $T_{1/2}^{q_i}$ are discussed below. For a neutral atom $q_i = Z$.

The total decay constant is the sum of the decay constant for gamma decay and electron conversion:

$$\lambda_{tot} = \lambda_{\gamma} + \lambda_{e-} = \lambda_{\gamma}(1+\alpha_{tot}) = \frac{1}{\tau_{\gamma}} + \frac{1}{\tau_{e-}} = \frac{1}{\tau_{tot}} = \frac{ln2}{T_{1/2}^{tot}}, \tag{4.5.10}$$

from where we can determine

$$T^{tot}_{1/2} = T^{q_i=Z}_{1/2} = \frac{T^{\gamma}_{1/2}}{(1+\alpha_{tot})} \tag{4.5.11}$$

For a fully stripped ion $\lambda_{tot} = \lambda_{\gamma}$, and

$$T^{tot}_{1/2} = T^{q_i=0}_{1/2} = T^{\gamma}_{1/2} \tag{4.5.12}$$

For the analysis of data from the fission experiments, where lighter nuclei were studied ($Z = 47-52$), the FRS can be divided in two sections from this point of view. As pointed out in Section 4.2, 99% of the selected ions are fully stripped even after passing the S2 wedge degrader. Thus all ions will be considered as fully stripped from the target to the S4 vacuum window, and all ions will be considered as neutral after the vacuum window of the FRS. However, in the fragmentation experiment, where much heavier nuclei were transmitted, the corresponding probability of an ion being fully stripped in the region between the target and S2 degrader, and between S2 and S4 were typically about 96% and 88% respectively, as pointed out in Paper V.

The experimental results can be compared with isomeric ratios predicted by theoretical models. The abrasion-ablation model has been applied [43] to describe the distribution of angular momenta populated in projectile fragmentation reactions. Using the model distributions the isomeric ratio can be calculated under the extreme simplifying assumption that R is equal to the probability that the final reaction product is produced with an angular momentum larger than that of the isomer. Results of such a comparison are available in Ref. [44], where the experimental isomeric ratios of neutron-rich isotopes in the Pb region produced by projectile fragmentation of ^{238}U are shown to be in very good agreement with the ones predicted by the model. Paper V presents results on the angular momentum population in the fragmentation of ^{208}Pb measured during Experiment I. The fragment angular momentum distribution populated in in-flight fission reaction is investigated below. The results are discussed in Section 6.4.

4.5 Production rates

The *observed rate* at S4, or the number of ions of a given species measured at S4 per incident beam particle is given by:

$$P_{obs/b.p.} = \frac{N^{tot}(ID)}{N_{b.p.}L/F} \ , \tag{4.6.1}$$

The number of ions implanted at S4, $N^{tot}(ID)$, was discussed in Section 4.4. The number of beam particles hitting the target, $N_{b.p.}$, is measured continuously by the SEETRAM detector (Section 3.2.1). L and F are the numbers of accepted and received events by the electronics and are continuously monitored during the experiment. L/F is a measure of the deadtime, which thus is defined as $(1 - L/F)$.

Another important quantity is the *production rate*, or the number of ions of a given species produced per incident beam particle. It can be calculated from:

$$P_{prod/b.p.} = \frac{P_{obs/b.p.}}{T_{(target-S4)}} \ , \tag{4.6.2}$$

The transmission from the target to S4, $T_{(target-S4)}$, is calculated by the MOCADI code.

The *observed rate* at S4 is in itself an important number for the experimentalist as it contains directly the measured transmission through the FRS. These rates will be discussed further in Section 6.5.

Chapter 5

Results

5.1 The ^{208}Pb fragmentation experiment

The results from the neutron-rich K-isomer experiment are summarized in Figure 5.1. During this experiment several production settings were investigated and many neutron-rich isotopes were identified varying from Tb (Z=65) to Hg (Z=80), with neutron numbers ranging between 100 and 126. There was one setting on the proton-rich side as well, centered around $^{140}_{66}$Dy. A number of known and new isomers with lifetimes from nanosecond to millisecond ranges were observed, e.g. the $K^{\pi} = 35/2^{-}$ isomers in ^{179}W [45], ^{175}Hf [46], and ^{181}Re [47]. This is the highest angular momentum observed to be populated in projectile fragmentation so far. The shortest lifetime measured in this experiment, belonging to the $K^{\pi} = 7^{-}$ isomer in ^{200}Pt, was 14 ns [48]. This time is much shorter than the flight time trough the separator. Our explanation is that this is due to the primary transition energy being less than the K-shell binding energy in platinum (78 keV). Thus the decay can only occur via electron conversion. Hence it is only when the ion is implanted in the catcher that the isomeric state can be depopulated and attain its natural half-life. A number of new isomers were discovered in this experiment and are indicated in Figure 5.1. Some new and very neutron-rich isotopes were also identified including ^{187,188}Ta, ^{191}W, ^{193,194}Re (see Paper I and Ref. [48, 26]), confirming the work of Reference [49].

The results of the isomeric ratios of the ^{208}Pb fragmentation experiment are presented in Paper V.

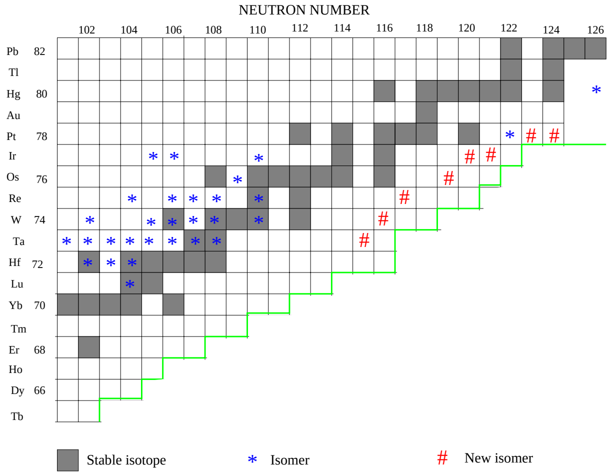

Figure 5.1: Part of the nuclidic chart showing the region which has been covered in the ^{208}Pb fragmentation experiment. The isomers known from before and observed also in our experiment are marked as well as the new isomers which have been observed for the first time in this experiment.

5.2 The ^{238}U fission experiments

5.2.1 Lifetime measurements of isomeric states

In the first ^{238}U fission experiment we covered three production settings, optimized for ^{131}Sn, ^{134}Sn and ^{130}Cd. During this experiment we observed some 35 isotopes in the neutron-rich Ag to Te isotopes with neutron numbers varying from 76 to 88. The first setting was aimed for calibration of the particle identification. In the second setting one new isomer was observed in ^{136}Sb (Paper III). In fact it was the first observation of an excited state in this isotope, which makes it the most neutron-rich Sb isotope from which γ-rays have been observed so far. The lifetimes of the new isomer, and of two previously known isomers were determined. The results are summarized in Table 1 in Paper III. In the last, most exotic setting, ^{136}Sn and ^{130}Cd were identified with about 1200 and 700 ions implanted in the aluminum catcher, respectively. However, no delayed γ-rays could yet be associated with these nuclei. In addition, we have indication for the observation of several new isotopes.

During the other two fission experiments (Experiments III and IV) we concentrated on two production settings optimized for ^{130}Sn and ^{127}In. Some 25 isotopes of Cd-Te were identified. A number of new isomers in Cd and In nuclei were discovered as shown in Figure 5.2, and their half-lives were measured, see Paper VI. The results on the In isotopes are summarized in Table 5.1. They will be discussed in Chapter 6.

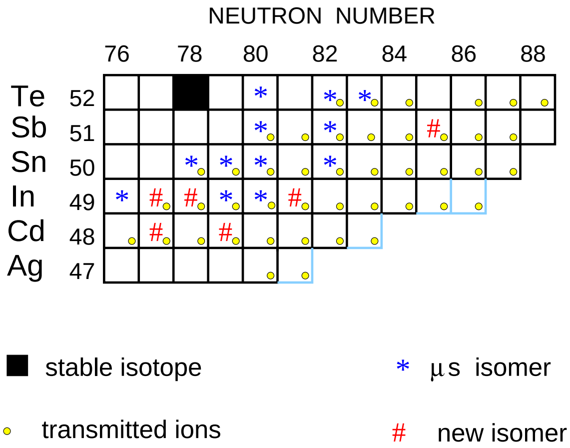

Figure 5.2: Part of the nuclidic chart showing the region covered in the ^{238}U fission experiments. All known μs isomers in the region, all isotopes and new isomers observed in this experiment are shown on the plot. For all the Cd and Ag isotopes in the plot, only the ground state has been observed so far. The grey squares represent candidates for isotopes potentially observed for the first time.

Table 5.1: Half-lives and γ-ray transitions associated with the antimony and indium isomers observed in the present study. The half-lives were obtained by fitting the decay time distributions of the γ-rays indicated in bold type.

Isotope	Observed delayed γ-rays [keV]	Half-life (μs) This work	Half-life (μs) Previous
^{136}Sb	**173**	0.57(5)	
^{125}In	**737, 1173**	13(4)	9.4(6) [50]
^{126}In	201, **244**, 614, 865	30(3)	
^{127}In	**221**, **233**	0.09(3), 13(2)	
^{128}In	**248**, 323	170(80)	>10 [51]
^{129}In	**332**, **358**, 994, 1352	11(2)	8.5(5) [52]
^{130}In	**389**	6(3)	
^{129}Sn	**382**, 570, 1136, 1324	3.9(4)	3.6(2) [53]
^{130}Sn	97, **391**	1.5(2)	1.61(15) [54]
^{134}Te	**297**	168 (12) ns	164 (1) ns [55]

5.2.2 Isomeric ratios

The isomeric ratios for some selected isomers were evaluated from the data measured during Experiments III.a (with a Be target) and III.c (with a Pb target). The results are summarized in Table 5.2. The overall uncertainty of this evaluation is estimated to be on the level of 20% and is mainly governed by the uncertainties of γ-ray efficiency determination and the integration of the γ-peaks. Isomers for which the decay scheme is known were predominantly chosen for the evaluation. However, preliminary isomeric ratios were derived for some cases, for which the multipolarities of some or all of the transitions following the primary isomer transition are unknown (^{129}Sn and ^{129}In, see Section 6.4 for details). For the new isomers observed in ^{127}In, lower and upper limits were defined. Table 5.3 summarizes the isomeric ratios for two isomers, measured during the momentum distribution scan (Experiment III.b). The uncertainty of the isomeric ratios corresponding to the beam energies of 753, 756 and 759 MeV/u is even larger, on the order of 30%, because of the low statistics collected in the measurements.

Table 5.2: Isomeric ratios measured during experiments III.a and III.c with Be and Pb targets, after in-flight fission of ^{238}U at 750 MeV/u and 732 MeV/u, respectively.

Nucleus	Isomeric I^{π}	E^{*}, keV	$T_{1/2}, \mu$s	$R(Be$ target)	$R(Pb$ target)
^{134}Te	6^{+}	1691	0.164	0.11	0.09
^{133}Sb	$> 17/2^{+}$	4526+x	16	0.04	0.03
^{131}Sb	$23/2^{+}$	2166.3	1.1	0.077	0.046
^{131}Sn	$23/2^{-}$	4846.7	0.3	0.026	0.015
^{130}Sn	5^{-}	2085	0.052	0.16	0.12
^{130}Sn	10^{+}	2435	1.6	0.11	0.07
^{129}Sn	$19/2^{+}$	1746	3.7	0.22*	0.09*
^{129}In	$17/2^{-}$	1688	8.5	0.21*	0.11*
^{127}In	–	–	0.09	$0.04 < 0.18$*	$0.05 < 0.25$*

** preliminary result. see Sect. 6.4 for details*

Table 5.3: Isomeric ratios measured during experiment III.b with the Be target, after in-flight fission of ^{238}U at different energies.

Nucleus	Isomeric I^{π}	E_{prim}, MeV/u	R
^{129}Sn	$19/2^{+}$	750	0.22
		753	0.17
		756	0.20
		759	0.14
^{131}Sb	$23/2^{+}$	750	0.08
		753	0.08
		756	0.11
		759	0.07

5.2.3 Production rates

The production and observed rates for some ions observed during Experiments III.a and III.c with both Be and Pb targets, as well as during the momentum distribution scan (experiment III.b) were calculated and are presented in Tables 5.4 - 5.9. The uncertainty of this evaluation is on the level of four percent and is mainly due to the uncertainty in defining the number of ions in the identification plot, $N^{tot}(ID)$.

Table 5.4: Production and observed rates measured during experiment III.a with a Be target, after in-flight fission of ^{238}U at 750 MeV/u, setting optimized for ^{130}Sn, $N_{b.p.} = 2.2 * 10^{12}$, the deadtime was 48 %.

Charge	Mass	$N^{tot}(ID)$	$T_{(target-S4)}$	$P_{obs/b.p.}$	$P_{prod/b.p.}$
52	132	100203	1.39E-3	8.7E-8	6.3E-5
52	133	478620	7.7E-3	4.1E-7	5.3E-5
52	134	398742	1.5E-2	3.4E-7	2.3E-5
51	130	324588	6.93E-3	2.8E-7	4.0E-5
51	131	912761	1.47E-2	7.9E-7	5.4E-5
51	132	1170450	2.64E-2	1.0E-6	3.8E-5
51	133	915388	3.57E-2	7.9E-7	2.2E-5
50	128	379274	1.05E-2	3.3E-7	3.1E-5
50	129	646670	2.16E-2	5.6E-7	2.6E-5
50	130	795122	3.29E-2	6.9E-7	2.1E-5
50	131	552511	3.48E-2	4.8E-7	1.4E-5
50	132	273003	3.28E-2	2.4E-7	7.9E-6
49	126	82358	6.6E-3	7.1E-8	1.1E-5
49	127	126177	1.78E-2	1.1E-7	6.1E-6
49	128	82312	2.91E-2	7.1E-8	2.4E-6
49	129	50286	3.07E-2	4.3E-8	1.4E-6

Table 5.5: Production and observed rates measured during experiment III.c with a Pb target, after in-flight fission of ^{238}U at 732 MeV/u, setting optimized for ^{130}Sn, $N_{b.p.} = 6.25 * 10^{11}$, the deadtime was 46 %.

Charge	Mass	$N^{tot}(ID)$	$T_{(target-S4)}$	$P_{obs/b.p.}$	$P_{prod/b.p.}$
52	132	20484	2.34E-4	6.1E-8	2.6E-4
52	133	135885	4.65E-3	4.0E-7	8.7E-5
52	134	190511	1.25E-2	5.6E-7	4.5E-5
51	130	55056	3.09E-3	1.6E-7	5.3E-5
51	131	246351	1.08E-2	7.3E-7	6.7E-5
51	132	452921	2.42E-2	1.3E-6	5.5E-5
51	133	404277	3.73E-2	1.2E-6	3.2E-5
50	128	67649	6.61E-3	2E-7	3.0E-5
50	129	178035	1.92E-2	5.3E-7	2.8E-5
50	130	284728	3.18E-2	8.4E-7	2.7E-5
50	131	196303	4.34E-2	5.8E-7	1.3E-5
50	132	68958	3.81E-2	2.0E-7	5.4E-6
49	126	11368	5.17E-3	3.4E-8	6.5E-6
49	127	24390	1.87E-2	7.2E-8	3.9E-6
49	128	18007	2.98E-2	5.3E-8	1.8E-6
49	129	8701	3.91E-2	2.6E-8	6.6E-7

Table 5.6: Production and observed rates measured during experiment III.c with a Pb target, after in-flight fission of ^{238}U at 732 MeV/u, setting optimized for ^{127}In, $N_{b.p.} = 2.0 * 10^{12}$, the deadtime was 33 %.

Charge	Mass	$N^{tot}(ID)$	$T_{(target-S4)}$	$P_{obs/b.p.}$	$P_{prod/b.p.}$
51	130	202826	3.3E-3	1.5E-7	4.6E-5
51	131	597797	1.07E-2	4.5E-7	4.2E-5
51	132	575385	1.91E-2	4.3E-7	2.3E-5
51	133	203020	1.15E-2	1.5E-7	1.3E-5
50	128	331772	7.85E-3	2.5E-7	3.2E-5
50	129	800945	2.04E-2	6.0E-7	2.9E-5
50	130	1114990	3.34E-2	8.3E-7	2.5E-5
50	131	628685	3.83E-2	4.7E-7	1.2E-5
50	132	156484	2.49E-2	1.2E-7	4.7E-6
49	126	151089	1.46E-2	1.1E-7	7.8E-6
49	127	190541	2.98E-2	1.4E-7	4.8E-6
49	128	117411	3.83E-2	8.8E-8	2.3E-6
49	129	45908	4.15E-2	3.4E-8	8.3E-7
48	124	3262	9.04E-3	2.4E-9	2.7E-7
48	125	18775	2.04E-2	1.4E-8	6.9E-7
48	126	16779	3.4E-2	1.3E-8	3.7E-7

Table 5.7: Production and observed rates measured during experiment III.b with a Be target, after in-flight fission of ^{238}U at 753 MeV/u, setting optimized for ^{130}Sn, $N_{b.p.} = 3.52 * 10^{11}$, the deadtime was 56 %.

Charge	Mass	$N^{tot}(ID)$	$T_{(target-S4)}$	$P_{obs/b.p.}$	$P_{prod/b.p.}$
52	132	34427	3.51E-3	2.2E-7	6.3E-5
52	133	103965	1.06E-2	6.7E-7	6.3E-5
52	134	85196	1.57E-2	5.5E-7	3.5E-5
51	130	68846	9.32E-3	4.4E-7	4.8E-5
51	131	161380	1.74E-2	1.0E-6	6.0E-5
51	132	193420	3.27E-2	1.3E-6	3.8E-5
51	133	142002	3.82E-2	9.2E-7	2.4E-5
50	128	68202	1.43E-2	4.4E-7	3.1E-5
50	129	104198	2.52E-2	6.7E-7	2.7E-5
50	130	118235	3.37E-2	7.6E-7	2.3E-5
50	131	80430	3.54E-2	5.2E-7	1.5E-5
50	132	38045	2.76E-2	2.5E-7	8.9E-6
49	126	12523	8.26E-3	8.1E-8	9.8E-6
49	127	17540	2.02E-2	1.1E-7	5.6E-6
49	128	11513	2.96E-2	7.4E-8	2.5E-6
49	129	6719	2.95E-2	4.3E-8	1.5E-6

Table 5.8: Production and observed rates measured during experiment III.b with a Be target, after in-flight fission of ^{238}U at 756 MeV/u, setting optimized for ^{130}Sn, $N_{b.p.} = 3.1 * 10^{11}$, the deadtime was 53 %.

Charge	Mass	$N^{tot}(ID)$	$T_{(target-S4)}$	$P_{obs/b.p.}$	$P_{prod/b.p.}$
52	132	60145	6.205E-3	4.1E-7	6.6E-5
52	133	129804	1.331E-2	8.9E-7	6.7E-5
52	134	99276	1.995E-2	6.8E-7	3.4E-5
51	130	91084	1.175E-2	6.2E-7	5.3E-5
51	131	183423	2.176E-2	1.3E-6	5.8E-5
51	132	199470	3.532E-2	1.4E-6	3.9E-5
51	133	136886	3.79E-2	9.4E-7	2.5E-5
50	128	80302	1.549E-2	5.5E-7	3.6E-5
50	129	110479	2.984E-2	7.6E-7	2.5E-5
50	130	115678	3.465E-2	7.9E-7	2.3E-5
50	131	75656	3.385E-2	5.2E-7	1.5E-5
50	132	33746	2.505E-2	2.3E-7	9.2E-6
49	126	13434	9.905E-3	9.2E-8	9.3E-6
49	127	17349	2.226E-2	1.2E-7	5.3E-6
49	128	10727	3.214E-2	7.4E-8	2.3E-6
49	129	5992	2.693E-2	4.1E-8	1.5E-6

Table 5.9: Production and observed rates measured during experiment III.b with a Be target, after in-flight fission of ^{238}U at 759 MeV/u, setting optimized for ^{130}Sn, $N_{b.p.} = 2.66 * 10^{11}$, the deadtime was 54 %.

Charge	Mass	$N^{tot}(ID)$	$T_{(target-S4)}$	$P_{obs/b.p.}$	$P_{prod/b.p.}$
52	132	79366	9.05E-3	6.6E-7	7.3E-5
52	133	136009	1.81E-2	1.1E-6	6.2E-5
52	134	99865	2.24E-2	8.3E-7	3.7E-5
51	130	103226	1.62E-2	8.5E-7	5.3E-5
51	131	181370	2.92E-2	1.5E-6	5.1E-5
51	132	179535	3.77E-2	1.5E-6	3.9E-5
51	133	114846	3.89E-2	9.5E-7	2.4E-5
50	128	81305	1.76E-2	6.7E-7	3.8E-5
50	129	101248	3.22E-2	8.4E-7	2.6E-5
50	130	100273	3.51E-2	8.3E-7	2.4E-5
50	131	63002	2.91E-2	5.2E-7	1.8E-5
50	132	25733	2.26E-2	2.1E-7	9.4E-6
49	126	12933	1.11E-2	1.1E-7	9.7E-6
49	127	14855	2.17E-2	1.2E-7	5.6E-6
49	128	8748	2.74E-2	7.2E-8	2.6E-6
49	129	4496	2.58E-2	3.7E-8	1.4E-6

Chapter 6

Discussion

6.1 K-isomers in the A =180-200 mass region

In the $A \approx 180$ mass region the nuclei are deformed and axially symmetric. Therefore, they are good rotors, i.e. they show collective rotational bands with excitation energies proportional to $I(I+1)$. The isomeric state is normally the band head of a rotational band and the isomer decays to a band with lower K. Since many valence particles contribute to the configuration of the K-isomeric state, it is difficult to perform shell-model calculations in an appropriate model space to explain the excitations in such nuclei.

For example, in the case of the newly observed γ-ray cascade in ^{190}W (see Fig. 2 in Paper I) we have performed blocked BCS (Bardeen–Cooper–Schrieffer) calculations in the way described in Ref. [16]. The quasi-particle energies and the strength of the pairing force were fitted to known states in the neighbouring ^{190,191,192}Os and ^{191}Re nuclei. The calculations suggest a low-lying two-quasiparticle state with $K^{\pi} = 10^{-}$ and a $\nu[505]9/2^{-} \otimes \nu[615]11/2^{+}$ Nilsson configuration.

An isomer with the same structure has been suggested in the $N = 116$ isotone ^{192}Os. The $N = 116$ isotones ^{192}Os and ^{194}Pt are well known examples of γ-soft nuclei [56, 57]. In a simple model, the ratio of the excitation energies of the first 4^{+} and 2^{+} states can be used to distinguish between an axially symmetric deformed rotor (for which the ratio is 3.33), a spherical vibrational nucleus (the ratio is 2.0), and a γ-soft nucleus (≈ 2.5). The deduced ratio of the energies of the 4^{+} and 2^{+} in ^{190}W is 2.72, which is close to the limit of 2.5 for a γ-soft nucleus [58, 59].

We have also performed configuration-constrained potential-energy-surface calculations, according to the mechanism of Ref. [60], for the $K^{\pi} = 10^{-}$ state in ^{190}W. The results, plotted in Fig. 4, Paper I, predict almost identical shapes for the isomeric state and the ground state, and suggest significant γ-softness, which is in agreement with the conclusion from the $4^{+}/2^{+}$ energy ratio.

Further examination of the ratio of the 4^+ and 2^+ energies in comparison with several even-even nuclei in the neighbourhood was done as illustrated in Fig. 5 in Paper I. The experimental data point for ^{190}W deviates strongly from the general trend. While the energies of the first two excited states of ^{190}W can be explained in terms of triaxiality, their ratio compared to the systematics is not fully understood. The question could be related to a breakdown of the $Z = 64$ shell gap for $N < 78$ and $N > 88$ [59, 61], and to the possibility of a sub-shell gap for proton number 76 proposed by Mach [62] in a discussion of the alteration of effective shell gaps in this neutron-rich region.

It should, however, be noted that the discussion above is based on the level scheme presented in Fig. 3, Paper I. The scheme was constructed on the basis of γ-ray singles information (the statistics did not allow a $\gamma\gamma$ coincidence analysis) and comparisons with neighbouring nuclei. It is therefore possible that the level ordering could be different.

6.2 Neutron-rich antimony isotopes

Figure 6.1 shows the neutron and proton single-particle levels around the $N = 82$ and $Z = 50$ closures. The lowest excitations for the nuclei having few valence particles or holes above or below the closures will be determined by the orbitals available for these valence particles (holes).

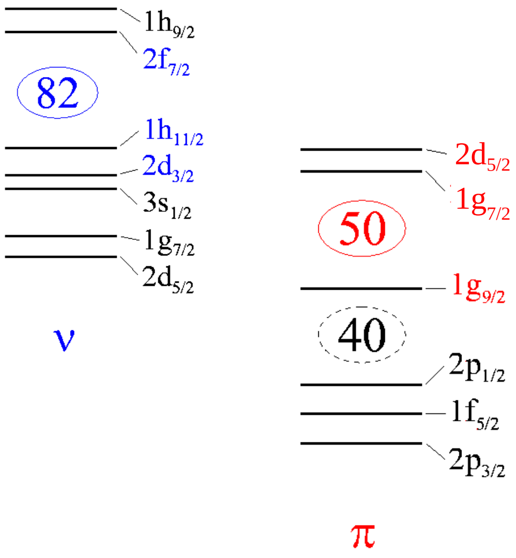

Figure 6.1: Single-particle orbitals for neutrons (ν) and protons (π) around the $N = 82$ and $Z = 50$ closures.

In nuclei around ^{132}Sn the coupling of the valence particles and holes occupying relatively high-j orbitals often gives rise to low-spin isomers. One example is the isomer newly identified in ^{136}Sb reported in Paper III.

The stiffness of the ^{132}Sn doubly-magic core promises that the single-particle states in the surrounding nuclei should be rather pure. In Paper III we investigate the development of the shell structure comparing the two valence particle nucleus ^{134}Sb (one proton and one neutron above the doubly-magic core) with the isotope ^{136}Sb, which has four valence particles. The development of collectivity and the role of high-j orbitals is discussed when adding a pair of neutrons. We performed shell model calculations for both ^{134}Sb and ^{136}Sb, using two different approaches - namely, the Kuo-Herling shell model (KHSM), and an empirical shell model (ESM). Two sets of interactions have been used to calculate the excitation energies for the lowest multiplets - $\pi \mathrm{g}_{7/2}\nu \mathrm{f}_{7/2}$ in ^{134}Sb, and $\pi \mathrm{g}_{7/2}\nu \mathrm{f}^{3}_{7/2}$ in the case of ^{136}Sb.

The results of the calculations are plotted in Figures 4 and 5 in Paper III. The KHSM model uses realistic two-body matrix-elements from the ^{208}Pb region but scaled down by $A^{-1/3}$ in the full $Z = 50$ to 82 and $N = 82$ to 126 model space with mixing. The empirical shell-model uses two-body matrix-elements from ^{210}Bi, scaled from the $\pi \mathrm{h}_{9/2}\nu \mathrm{g}_{9/2}$ multiplet to the $\pi \mathrm{g}_{7/2}\nu \mathrm{f}_{7/2}$ multiplet, and $\mathrm{f}^{2}_{7/2}$ two-body matrix-elements from ^{134}Sn. Pure configurations are assumed. Surprisingly, the KHSM and ESM calculations agree almost perfectly, both for ^{134}Sb and for ^{136}Sb. Therefore, mixing (KHSM) does not affect strongly the calculations. This means that if there were other orbitals involved in the lowest excitations in those two nuclei, their contribution should be very small, i.e., the configurations are rather pure. The agreement with the experimental data is very good in the case of ^{134}Sb. Since we observe only one γ-ray transition from ^{136}Sb it is difficult to compare the data with the calculations, but the ground state of $I^{\pi} = 1^{-}$ predicted by both calculations is in agreement with the ground state spin and parity deduced experimentally by Hoff *et al.* [63].

On the other side, the distribution of the level excitation energy as a function of angular momentum in the lowest multiplets looks very different for the two nuclei. While for ^{134}Sb the lowest and the highest spin members of the multiplet are lower in excitation energy relative to most of the levels in between, the corresponding states are located higher in ^{136}Sb and the level distribution is nearly flat. This 'parabola', which flattens from ^{134}Sb to its neighbour ^{136}Sb, reminds very much on the behaviour of the lowest multiplets in the corresponding counterparts in the ^{208}Pb region, ^{210}Bi and ^{212}Bi, discussed by Alexa *et al.* [64]. The authors study the reverse of the energy versus spin parabola as one goes from ^{210}Bi by adding pairs of neutrons and/or protons to ^{212}Bi, ^{212}At, ^{216}At, ^{216}Fr. With and without mixing they calculate the sequence of shell-model configurations in these odd-odd nuclei. The calculations without mixing show that the parabolic structure reverses as one goes from particle-particle configurations to particle-hole or hole-particle configurations. We expect that in the neighbouring odd-odd antimony isotopes with larger neutron excess, with the increasing occupation of the neutron $f_{7/2}$ orbital, the particle-particle proton-neutron interaction in ^{134}Sb will change into a particle-hole interaction in ^{140}Sb, which will invert the parabola distribution via the rather flat distribution calculated for ^{136}Sb.

6.3 Level structure and decay properties of odd-mass indium isotopes

The indium isotopes have one proton hole in the $1g_{9/2}$ or $2p_{1/2}$ orbital below the Z=50 closed shell and n neutron holes in the $1h_{11/2}$, $2d_{3/2}$ or $3s_{1/2}$ orbitals below the N=82 closed shell (n lies between 6 and 1 for $^{125-130}$In). The presence of odd nucleons in these relatively high-j orbitals makes it possible to form a large number of states of different intrinsic structure, organized in multiplets. The character and composition of the multiplets in many cases results in appreciable hindrance factors, both for intramultiplet transitions and for those connecting levels belonging to different multiplets. For this reason the neutron-rich indium isotopes "south-west" of doubly magic ^{132}Sn are very rich in isomeric states, both β-decaying isomers with half-lives around a second and above, as well as shorter-lived ones in the millisecond-to-microsecond range which decay preferably by γ emission.

As in the case of ^{136}Sb discussed in the previous section, the purity of the single-particle configurations is expected to decrease as the number of valence holes compared to the ^{132}Sn core increases. Thus a comparison of how the level structure changes when moving along the chain of indium isotopes is expected to give interesting insights into the growing importance of more collective degrees of freedom. It also sets up a formidable challenge to nuclear models to correctly reproduce not only the excitation energies of excited states in these nuclei but especially to accurately reproduce transition rates.

Table 6.1: Deduced properties, including spin/parity and half-life, for the primary isomeric transitions in the observed indium isomers. All data are taken from the present study, unless otherwise indicated.

Isotope	Primary isomeric transition			
	Energy [MeV]	Half-life [μs]	Proposed spin and parities $I_i^\pi \rightarrow I_f^\pi$	Multipolarity
^{125}In	0.050	13(4)	$19/2^+ \rightarrow 17/2^-$	E1
^{127}In	<0.050	13(2)	$29/2^+ \rightarrow 25/2^+$	E2
^{127}In	0.221/0.233	0.09(3)	$25/2^+ \rightarrow (23/2, 25/2)^-$	E1
^{129}In	0.332	11(2)	$17/2^- \rightarrow 13/2^+$	M2

In the following, our recent results on isomeric states in the odd-mass indium nuclei ^{125}In, ^{127}In and ^{129}In will be discussed. A summary of the decay data of the investigated isomeric states, including energies of the observed delayed γ-rays and half-lives determined for selected transitions, is provided in Table 5.1. Preliminary results from the analysis of the data from Experiments III.c and IV (see Table 3.1), including also new information on the even-mass nuclei ^{126}In, ^{128}In and ^{130}In, have been published in Paper VI and Ref. [65]. A complete discussion, together with results from an on-going shell model investigations of the region, can be found in Ref. [41]. In addition, our results on isomers in ^{125}Cd and ^{127}Cd will be published separately [66].

Figures 6.2 and 6.3 illustrate γ-ray energy spectra of ^{125,127,129}In, and decay time distributions for selected delayed transitions. Table 6.1 lists deduced nuclear structure information, while Figure 6.4 contains partial level schemes. As many aspects of the intrinsic structure of the odd-mass indium nuclei can be understood in terms of the coupling of valence proton holes to core states in the neighboring even-mass tin systems, Figure 6.5 has been included for clarity.

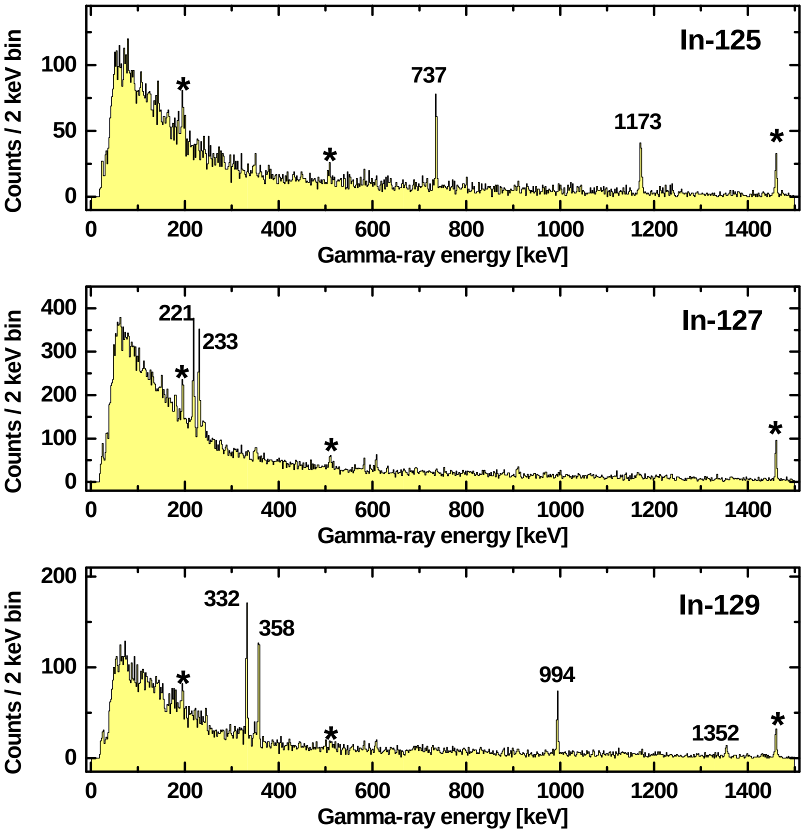

Figure 6.2: Heavy-ion–gated delayed (0-60 μs after prompt) γ-ray spectra of selected odd-mass indium isomers. Asterisks label transitions associated with background activities.

6.3.1 Results for ^{129}In and ^{125}In

^{129}*In*

In comparison to doubly magic ^{132}Sn, ^{129}In has one hole in the $g_{9/2}$ proton shell and two neutron holes, most likely of $d_{3/2}$, $h_{11/2}$ or $s_{1/2}$ character. Several β-decaying states are known [50], including the I^{π}=9/2^{+} ground state, a low-lying 1/2^{-} state

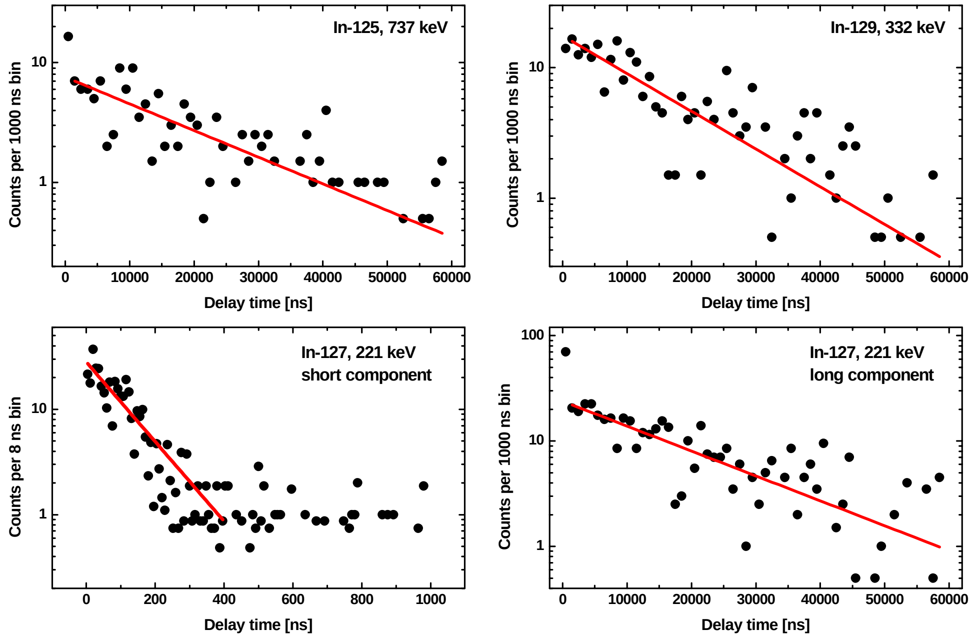

Figure 6.3: Background-subtracted time distributions obtained for selected transitions associated with the decays of isomeric states in odd-mass indium fission fragments. In the case of ^{127}In, data from both Experiment III.c (short component) and Experiment IV (long component) are shown. The solid lines indicate single exponential-component fits to the data, see Table 5.1.

and, as recently reported [67], a high-lying $23/2^-$ state. The existence of the latter had previously been put forward in connection with the discovery of a 700(30) ms M2/E3 isomeric transition thought to connect the expected maximally-aligned $29/2^+$ state with the $23/2^-$ level [50]. The confirmation [67] of the spin and parity of the high-lying β-decaying state thus also validates the assignment of the $29/2^+$ level, which is formed by the coupling of the $g_{9/2}$ proton hole and the 10^+ ^{130}Sn core state.

A comparison with ^{130}Sn shows that in that nucleus, the 10^+ state, although isomeric because of the relatively small energy difference of just 97 keV, is able to decay to the lower-lying 8^+ state [54]. In ^{129}In, however, this possibility is clearly not open as the $29/2^+$ state is forced to decay to the $23/2^-$ level, implying that the expected $25/2^+$ must be situated slightly above the $29/2^+$ level. The long half-life of the $29/2^+$ state is thus due to a true spin-gap effect.

Complementary to these states, Genevey *et al.* [53] have observed several γ-transitions decaying with a common $T_{1/2}$=8.5(5) μs. A later study [52] by the same group assigns I^π=$17/2^-$ to the isomeric state, based on systematics of the region as well as shell model calculations. We observe the same γ-transitions as reported by Genevey *et al.* [52, 53]. Although our half-life of 11(2) μs is slightly longer, our result is in good agreement with the previously reported value.

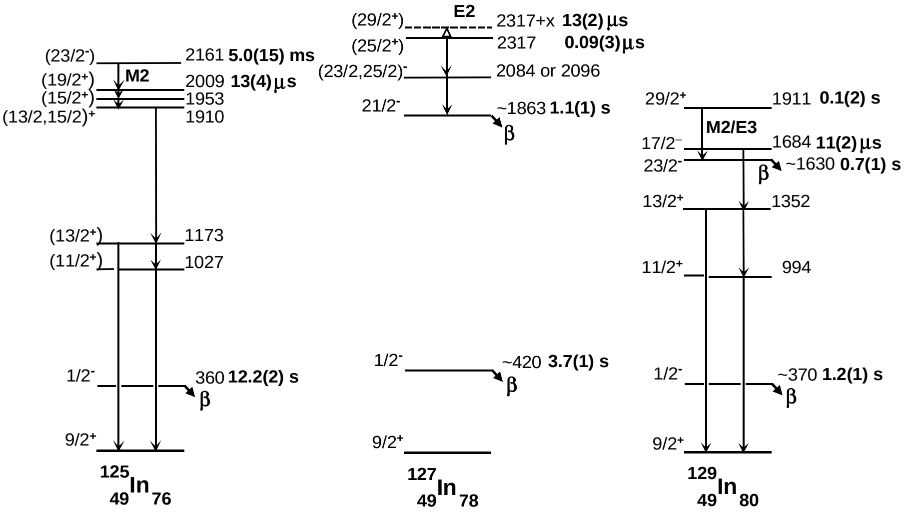

Figure 6.4: Schematic level schemes for selected odd-A indium nuclei. Spin/parity assignments and microsecond-range half-lives refer to our work (see text for details), while level energies and other half-lives have been taken from Refs. [50] (^{125}In), [67, 68] (^{127}In) and [52, 67] (^{129}In).

The deexcitation pattern of Refs. [52, 53] is indeed consistent with the decay of a I=17/2 state, as any higher spin would not allow for the known 700 ms ($23/2^-$) β-decaying isomer observed by Fogelberg *et al.* [50]. A positive parity would enable a fast E2 transition to the $13/2^+$ state at 1352 keV, thus destroying the observed isomerism. The existence of an undetected low-energy E1 primary isomeric transition cannot be excluded from our data, but this option appears highly unlikely as the conversion electron spectroscopy performed by Genevey *et al.* failed to provide any evidence for such a (highly converted) transition.

^{125}*In*

^{125}In is situated further away from ^{132}Sn than ^{129}In, and it is therefore expected that its states will be built up from combinations of several different orbitals rather than be dominated by pure configurations. Important proton orbitals include $p_{1/2}$ and $g_{9/2}$, whereas the six valence hole neutrons have $d_{3/2}$, $h_{11/2}$ or $s_{1/2}$ character.

Early β-decay work has revealed two low-lying β-decaying levels, the $9/2^+$ ground state and a $1/2^-$ state at 360 keV [69]. The latter is thought to have a large contribution of the $p_{1/2}$ proton orbital in its wave function [70]. In addition to these isomers, Fogelberg *et al.* [50] have reported the existence of two higher-lying isomeric levels that decay by emission of γ-rays and conversion electrons. The authors observed a 152 keV M2 γ-ray with a half-life of 5.0(15) ms, which was interpreted as connecting a ($23/2^-$) state at 2161 keV with a lower-lying level at 2009 keV, tentatively assigned spin I=(19/2,21/2). The 2009 keV level is in itself isomeric, with a half-life of 9.4(6) μs. The conversion electron spectroscopy data of Ref. [50] show that the isomer decay proceeds via a cascade initiated by two low-energy, highly converted transitions. The 56 keV E2 primary isomeric transition is followed by a 43 keV M1 transition, and the sequence ends in the $9/2^+$ g.s. via two transitions with relatively high energy, 737 and 1173 keV.

Although our experimental setup was insensitive both to low-energy γ-rays and to conversion electrons, we do observe the two latter coincident transitions. The average half-life of the two transitions comes out as 13(4) μs – slightly longer than the value of Ref. [50], but still in relatively good agreement. It is interesting to note that, in analogy with ^{127}In (see below), the decay time distribution of the 737 keV transition appears to exhibit two components – in addition to the long half-life discussed above, the elevated number of counts in the first time bin hints at the presence of a second, much shorter decay. Unfortunately our data precludes a closer investigation of this phenomenon, but it remains an intriguing possibility.

As mentioned above, Fogelberg *et al.* [50] have proposed a spin and parity of $(23/2^-)$ for the ms-isomeric level at 2161 keV . Such a state is expected in the vicinity of 2 MeV, where it can be formed by the maximal alignment of a $g_{9/2}$ proton hole coupled to the $\nu d^{-1}_{3/2} h^{-1}_{11/2}$ $I^\pi=7^-$ two-quasi-neutron state. These 7^- states are well-known in the neighboring even-mass tin isotopes, see Figure 6.5. Since the 4^+ and 5^- states lie below the 7^- level in ^{126}Sn, it is natural to assume that the corresponding $23/2^-$ level in ^{125}In should be able to γ-decay to lower-lying states with spins in the range I=13/2 – 21/2, as is indeed observed.

However, the proposed assignment of I=21/2 for the 2009 keV level [50], which implies a $\Delta I = 1$ M2 transition from the $23/2^-$ isomer, seems less well founded. The systematics of the region, as well as relatively simplistic shell model calculations performed by us, lead us to propose that the M2 isomeric transition is more likely to have $\Delta I = 2$ character, requiring I=19/2 for the 2009 keV state.

The exact nature of the $19/2^+$ state is difficult to ascertain, as the coupling of a 4^+ state, as found in the even Sn "core", and a $g_{9/2}$ proton can maximally result in $I^\pi=17/2^+$. To form a $19/2^+$ state thus requires that the valence proton hole couples to a $(5,6)^+$ state in ^{126}Sn, which involves the $g_{7/2}$ orbit. In the lighter indium isotopes, such states normally occur at higher excitation energy. However, ^{125}In lies in a region where both $\nu g_{7/2}$ and $\pi g_{9/2}$ are holes and thus can interact strongly as they are spin-orbit partners, thereby lowering the coupled states.

Concerning the decay out of the 2009-keV level, the 56 keV E2 transition is most likely to be stretched, implying $\Delta I = 2$, as any M1 component would increase the total transition rate and therefore destroy the isomerism. Consequently, the state at 1953 keV should be assigned I=15/2, resulting in the 43 keV M1 being of $15/2^+ \rightarrow (13/2,15/2)^+$ character. Considering the configurations involved, a positive parity is most likely.

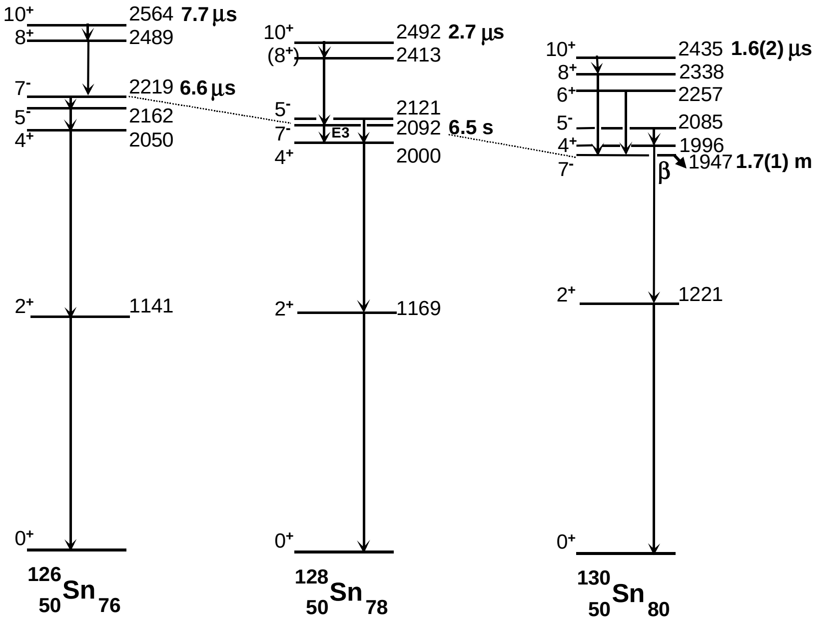

Figure 6.5: Schematic level schemes for selected tin nuclei. The data have been taken from Refs. [71] (^{126}Sn), [54, 72] (^{128}Sn) and [54] (^{130}Sn).

6.3.2 New data on ^{127}In

With its four neutron valence holes compared to the ^{132}Sn core, ^{127}In is situated in between its isotopes ^{125}In and ^{129}In, and one could expect that all three indium nuclei should exhibit many common features. Indeed, previous studies of the β-decay of ^{127}Cd [70, 73] strongly suggest the ground state of ^{127}In to have $I^{\pi}=9/2^{+}$, and similarly to its odd-mass neighbors, a β-decaying $1/2^{-}$ state was found at around 460 keV. Gausemel *et al.* [67] have recently reported the existence of a higher-lying β-decaying isomeric state at 1863(56) keV, which they assign as $I^{\pi}=21/2^{-}$. Hoff *et al.* [68] made a detailed γ-spectroscopic study of levels in ^{127}In populated in the β-decay of the ^{127}Cd $I^{\pi}=(3/2)^{+}$ ground state, and were able to identify a number of excited states located on top of both the ground state and the $I^{\pi}=1/2^{-}$ isomer. However, no states with half-lives in the microsecond-range have previously been reported in ^{127}In.

We observe two delayed γ-rays with 221 and 233 keV, which both exhibit decay time distributions consistent with the presence of two decay components, one short and one long. The preliminary analysis of the data from Experiment III.c indicated the half-life of the fast component to be < 150 ns, but the fit was made difficult by the presence of the second component, which was estimated to have a lifetime of the same order as the total time range recorded, i.e. 8 μs. The 10 times longer decay time range of Experiment IV allowed us to determine the long decay component to have $T_{1/2}$=13(2) μs. (In this time distribution, the short component manifested itself as a high number of counts in the first 500 ns, see Figure 6.3.) Using this value, the data from Experiment III.c were fitted one more time, resulting in $T_{1/2}$=90(30) ns for the short component. Analysis of the γ-spectroscopic data further show that the two transitions are coincident with each other.

This decay pattern, which at first sight shows little resemblance to the odd-A neighbors ^{125,129}In (see Figure 6.2), is thus a strong indication of the presence of two γ-decaying isomeric states. The fact that none of the transitions reported by Hoff *et al.* [68] are present in the delayed γ-ray spectrum seem to suggest that these isomers, as well as the levels populated in their decay, have an intrinsic structure that is inherently quite different from the states populated in the ^{127}Cd β-decay. Instead, it seems probable that this new level structure should be located at relatively high excitation energy, e.g., above the $I^{\pi}=21/2^{-}$ β-decaying isomeric state at 1863(56) keV.

We propose that the longer half-life is due to a low-energy, highly converted E2 $(29/2^{+})\rightarrow(25/2^{+})$ transition which, because of the lower detection limit of $\approx$ 70 keV, was not observed in our experiment. Starting from the known B(E2;$10^{+} \rightarrow 8^{+}$) = 0.37(3) W.u. for ^{128}Sn, which in the stretched coupling limit should be identical to the B(E2;$29/2^{+} \rightarrow 25/2^{+}$) in ^{127}In, it is possible to deduce a limit for the energy of the non-observed γ-ray: $E_{\gamma}^{5} * (1 + \alpha_{tot}) = 5.656 * 10^{-4}/(B(E2)*T_{1/2})$, with E_{γ} in keV, B(E2) in e^2fm^4, $T_{1/2}$ in μs and α_{tot} is the total conversion coefficient. From this we obtain $E_{\gamma} < 35$ keV, which is reasonable. This situation can be compared to the considerably slower decay of the $29/2^{+}$ state in ^{129}In which, as discussed above, is a true spin-gap effect, in that the proton-neutron interaction favors the stretched configuration with the best spatial overlap. When moving into the neutron shell this effect fades away, and the $25/2^{+}$ may certainly move down again to sit below the $29/2^{+}$ already in ^{127}In.

The isomer with the short half-life must be located below the long one, as otherwise it should not be observable. It appears highly likely that one of the observed γ-rays is the primary isomeric transition, but as they are so similar in energy – 221 keV and 233 keV, respectively – it is not possible to pinpoint which one. The observed half-life is only compatible with E1 or E2 multipolarity, which would limit the spin and parity of the intermediate state to either $21/2^{+}$ or $(23/2,25/2)^{-}$, as other states are not foreseen by the shell model. The second of the two transitions would then connect the intermediate state with the $I^{\pi}=21/2^{-}$ β-decaying isomeric state at 1863(56) keV.

Can our data be used to distinguish between the two possibilities outlined above? Starting with the E2 alternative, we note that the B(E2;$25/2^{+} \rightarrow 21/2^{+}$) transition rate is, in the fully stretched limit, equal to the B(E2;$8^{+} \rightarrow 6^{+}$) value in ^{128}Sn. The latter value, although not known experimentally, can be calculated in the seniority scheme from the known ^{128}Sn B(E2;$10^{+} \rightarrow 8^{+}$)=0.37(3) W.u. by simple Racah 6j-symbol algebra: B(E2;$8^{+} \rightarrow 6^{+}$) = 2.669*B(E2;$10^{+} \rightarrow 8^{+}$)= 0.98(8) W.u. The resulting B(E2;$25/2^{+} \rightarrow 21/2^{+}$) corresponds to a half-life of 27 ns, which is clearly shorter than the experimental value of 90(30) ns.

The E1 alternative, on the other hand, implies I^{π}=$(23/2,25/2)^-$ for the intermediate state, and hence M1 or E2 multipolarity, respectively, for the second member of the cascade. The presence of a second excited 7^- state with a similar excitation energy in the core nucleus ^{128}Sn lends support to a $23/2^-$ assignment, but one would also expect a $\nu h_{11/2}d_{5/2}$ 8^- state in the vicinity, which would correspond to a $25/2^-$ level in ^{127}In.

Finally some comments on the probable locations of the expected $23/2^-$ and $17/2^+$ states in ^{127}In. As we have seen in the discussion above, the large spin gap forces the $23/2^-$ state in ^{129}In to β-decay rather than to deexcite via γ emission. In the case of ^{127}In, a comparison with ^{128}Sn leads us to expect the $23/2^-$ spin trap to exist, but instead of β-emission its decay may proceed through a long-lived E3 transition to the $17/2^+$ level. The half-life would certainly be too long for it to have been observed in our experiments, which were optimized for lifetimes in the 0.1-40 μs range. When it comes to the position of the ^{127}In $17/2^+$ level, the fact that the $21/2^-$ level is a β-decay trap with $T_{1/2}$=1.04(10) s makes unlikely, but not impossible, the existence of a competing M2 γ-ray branch to a such a $17/2^+$ state. However, this would require a large retardation of about $5 * 10^{-5}$ W.u. for this up to now unobserved transition, if we assume an energy of 50 keV. The conclusion is therefore that the expected $17/2^+$ is located less than about this energy below or above the $21/2^-$ isomer, which can be compared to the relative positions of the 4^+ and 7^- states in ^{128}Sn.

6.4 Angular momentum distribution of fission fragments

6.4.1 Isomeric ratios

The isomeric ratios of 9 isomers observed during Experiment III were evaluated. For each isomer, the isomeric ratio R (eq. 4.5.8.) was calculated for each transition belonging to the isomer decay, observed in our experiment. Table 6.2 summarizes some data relevant to the evaluation of the isomeric ratios. References to the sources of information are given.

For most of the considered cases the decay scheme of the isomer is known. There are some isomers, however, for which the multipolarities of some or all transitions following the primary isomer transition are unknown. Since the total conversion coefficient α_{tot} depends on the multipolarity of the transition, $\alpha_{tot} = 0$ has been used in the calculations for these cases, and only a preliminary result can be given in the present situation.

Even more complicated is the case of ^{127}In. Two new isomers were observed in this nucleus. For simplicity, the isomeric ratio was calculated assuming the short-lived isomer. The branching ratios were assumed to be equal to 1 and the total conversion coefficients α_{tot} were assumed to be equal to 0 for the transitions of 221 and 233 keV. Since there is no information on the primary isomer transition, in-flight

Table 6.2: Summary of experimental data involved in the evaluation of the isomeric ratios. For simplicity only the isomeric ratios measured with the Be target are presented here.

Isotope	E_γ	Multipolarity	$T_{1/2}^{q_i=Z}$	$T_{1/2}^{q_i=0}$	b_γ	$1 + \alpha_{tot}$, [42]	R
^{134}Te	115.2*	E2	164 ns	334.4 ns	1	3.55	
[74], [75]	297	E2			1	1.04	0.12
	1279	E2			1	1	0.098
^{133}Sb	10-20*	E2	16 μs	2.7 ms	1	166	
[76], [77]	162	M1			1	1.02	0.04
	1510	E1			1	1	0.037
^{131}Sb	96.4*	E2	1.1 μs	2.4 μs	1	2.2	
[78]	343	E1			0.63	1	0.084
	382	E2			0.37	1.02	0.069
^{131}Sn	158.4*	E2	300 ns	395 ns	1	1.32	0.024
[79], [80]	173.2	E1			1	1.04	0.027
^{130}Sn	89.2*	E1	52 ns	65.1 ns	1	1.25	
[54]	774.4	E2			1	1	0.11
^{130}Sn	96.5*	E2	1.6 μs	4.5 μs	1	2.8	
	391	E1			1	1	0.16
^{129}Sn	40*	E2	3.7 μs	171 μs	1	46.1	
[81]	382	unknown			1	1	0.21
	570	unknown			1	1	0.24
	1136	unknown			1	1	0.24
	1323	unknown			1	1	0.19
^{129}In	332*	M2	8.5 μs	9.2 μs	1	1.1	0.2
[52]	358	unknown			0.75	1	0.21
^{127}In	221	unknown	90 ns	infinite	1	1	$0.05 < 0.18$
	233	unknown			1	1	$0.03 < 0.13$

** primary isomer transition*

decay cannot be taken into account properly, and only upper and lower limits of the isomeric ratio can be given. Assuming $\alpha_{tot} = 0$ for the primary isomeric transition gives an upper limit of the isomeric ratio of R=0.18 (for the 221 keV transition) and R=0.13 (for the 233 keV transition). Assuming an infinite $T_{1/2}^{q_i=0}$ gives a lower limit of R=0.047 and R=0.034, respectively. When available, data on the branching ratios and multipolarities will improve these numbers.

6.4.2 Angular momentum distribution

The isomeric ratios, R, derived for all 9 isomers from the data measured with the Pb target are plotted in Figure 6.6 versus the spin I of the isomeric state. Note that for the $T_{1/2} = 90$ ns isomer in ^{127}In no spin assignment is available, and for the $T_{1/2} = 16$ μs isomer in ^{133}Sb the spin is believed to be greater than $17/2^+$ (see Table 5.2). The ratios follow a general trend of becoming lower with increasing angular momentum. However, the angular momentum involved in relativistic fission is not well understood and no theoretical calculations are available to compare with.

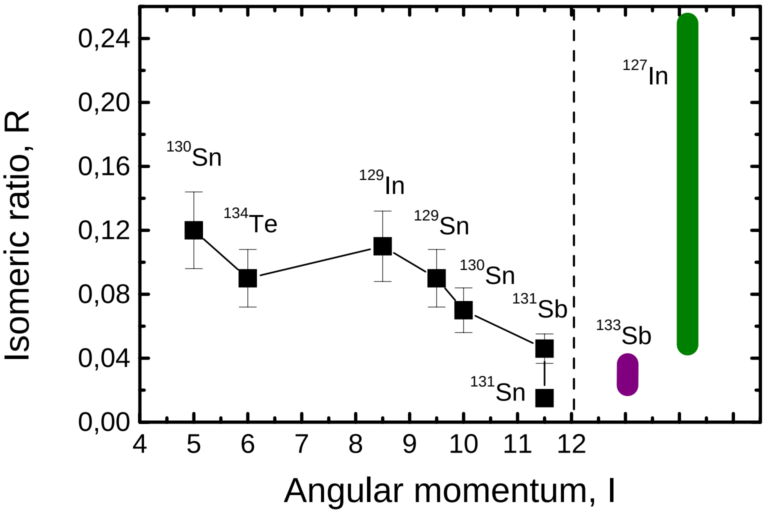

Figure 6.6: Isomeric ratios measured during experiment III.c (with Pb target) versus the angular momenta of the isomers. Only limits for the ratio can be given for the new isomer in ^{127}In. The value derived for the isomer in ^{133}Sb is in agreement with the spin being higher than $17/2^+$.

6.4.3 Comparison between the Be and Pb targets

The isomeric ratios measured with the Be and Pb targets were presented in Table 5.2. The results are plotted on Figure 6.7. Clearly the isomeric ratios measured with the Be target are higher than those measured with the Pb target. This is not surprising taking into account the different character of fission when a light or heavy target is used (see Section 3.1.2). The isomeric levels could be populated directly in the reaction, and/or could be fed by other structures above them, populated in the reaction. The experimental result that higher isomeric ratios have been observed with the Be target indicates that in general higher angular momenta are populated in the nuclear interaction for the U/Be system, than in the electromagnetic induced fission for the U/Pb system.

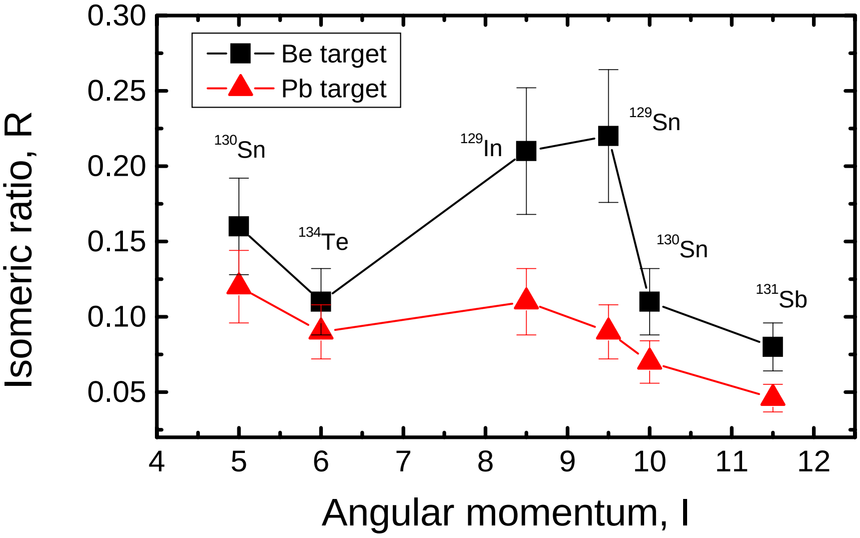

Figure 6.7: Isomeric ratios measured during experiments III.a (Be target, square symbols) and III.c (Pb target, triangles).

The values measured with the two targets for the isomers in ^{129}In and ^{129}Sn are diverging more than for the rest of the cases. Interestingly, these are isomers for which still certain questions exist in terms of multipolarities, as pointed out before. This could indicate that the level schemes of these nuclei are more complicated than the present understanding, e.g. the existence of other isomers above the ones reported, but poputaled differently in the different targets.

6.4.4 Momentum distribution scan

The broad momentum distribution of fission fragments and the rather narrow acceptance of the FRS was described in Section 3.1.2. In order to find the most efficient way to select fission fragments a scan in the momentum distribution was done. The isomeric ratios of two isomers, the $I^\pi = 19/2^+$ isomer in ^{129}Sn, and the $I^\pi = 23/2^+$ isomer in ^{131}Sb, were evaluated for each step in the scan. The results were presented in Table 5.3, and are plotted in Figure 6.8. The distribution of the isomeric ratios measured in the scan is rather flat within the error bars for the case of ^{131}Sb. In the case of ^{129}Sn there is an indication of a lowering the isomeric ratio with increasing the primary beam energy, which in practice corresponds to selecting fragments with lower velocity.

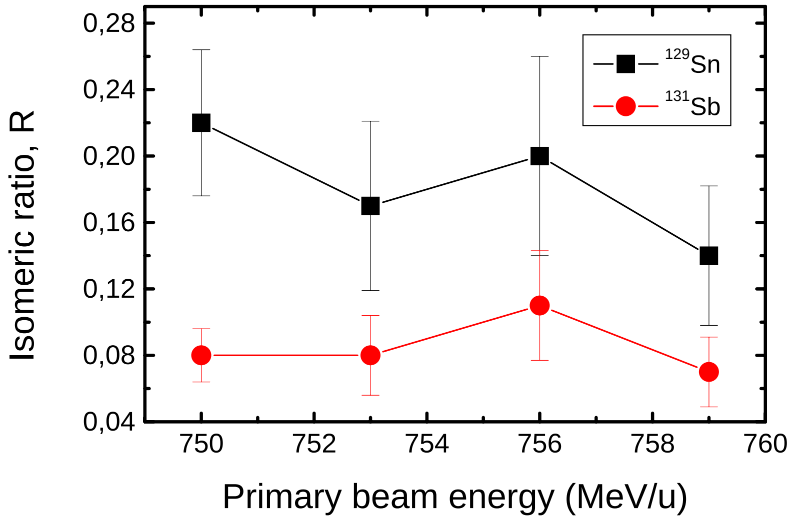

Figure 6.8: Isomeric ratios for the $I^{\pi} = 19/2^{+}$ isomer in ^{129}Sn, and the $I^{\pi} = 23/2^{+}$ isomer in ^{131}Sb measured during Experiment III.b (Be target) at different primary beam energies.

6.5 Production rates

6.5.1 Production rates measured with Be and Pb targets

The production and observed rates measured during Experiments III.a and III.c were presented in Tables 5.4, 5.5 and 5.6. The results for Sb, Sn and In isotopes are plotted in Figure 6.9. Three sets of measurements were done, one with a Be target during the production setting optimized for ^{130}Sn (Experiment III.a), one with a Pb target during the setting optimized for ^{130}Sn, and one with a Pb target, during the setting optimized for ^{127}In. Each pannel in Figure 6.9 contains data measured during the three measured sets for the isotopes of a given element.

Let us first concentrate on the data measured with the Pb target. Figures 6.9 a), c) and e) are easy to understand. They show that higher rates of Sb isotopes were observed at S4 during the setting optimized for ^{130}Sn, then during the setting optimized for ^{127}In, and vice versa for In ions, as expected. The production rates, however, should not depend on the setting since the only difference between the two settings was in the thickness of the S2 degrader. It can be seen in Figure 6.9 b) that the production rates for the Sb isotopes measured during the two settings diverge a lot, while they are almost the same for the Sn and In isotopes (Fig. 6.9 d) and f)). This means that the transmission from the target to S4, simulated in the MOCADI code,

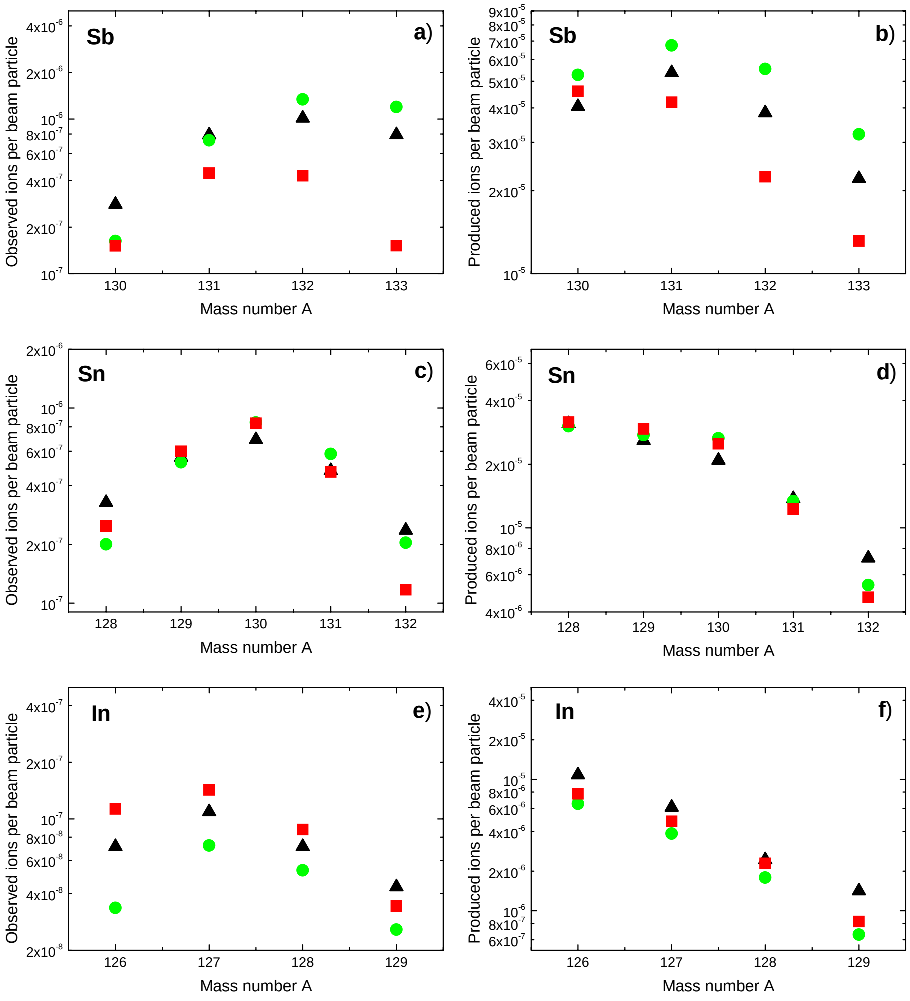

Figure 6.9: Observed and production rates measured during Experiments III.a and III.c. The triangles represent data measured with a Be target during the setting optimized for ^{130}Sn, the circles correspond to data measured with a Pb target during the setting optimized for ^{130}Sn, and the squares represent data measured with a Pb target during the setting optimized for ^{127}In. The four percent uncertanty is smaller then the size of the symbols in the plots.

is not correct for fragments far from the setting fragment. If one now compares the production rates measured with the Be and Pb targets, one can see no pronounced difference for the Sn isotopes, and somewhat higher production rate for the In ions with the Be target than with Pb target, but no major conclusion can be done.

6.5.2 Momentum distribution scan

The production and observed rates measured during the momentum distribution scan (Experiment III.b) were presented in Tables 5.4, 5.7, 5.8, and 5.9. The results are plotted in Figure 6.10. All measurements were done with the Be target during the setting optimized for ^{130}Sn at four primary beam energies. Clearly the observed rates for all Te isotopes are increasing with increasing the primary beam energy. For Sb, Sn and In isotopes the situation is different. The observed rates are increasing with the primary beam energy for the lighter isotopes, but there is a crossing point for each element after which the relation between observed ratios and primary beam energy changes its direction. Let us remember that a lower beam energy corresponds to selection of fragments with higher momentum/velocity (Section 3.1.2). This means that the exotic isotopes are selected better when choosing the high velocity part of the momentum distribution.

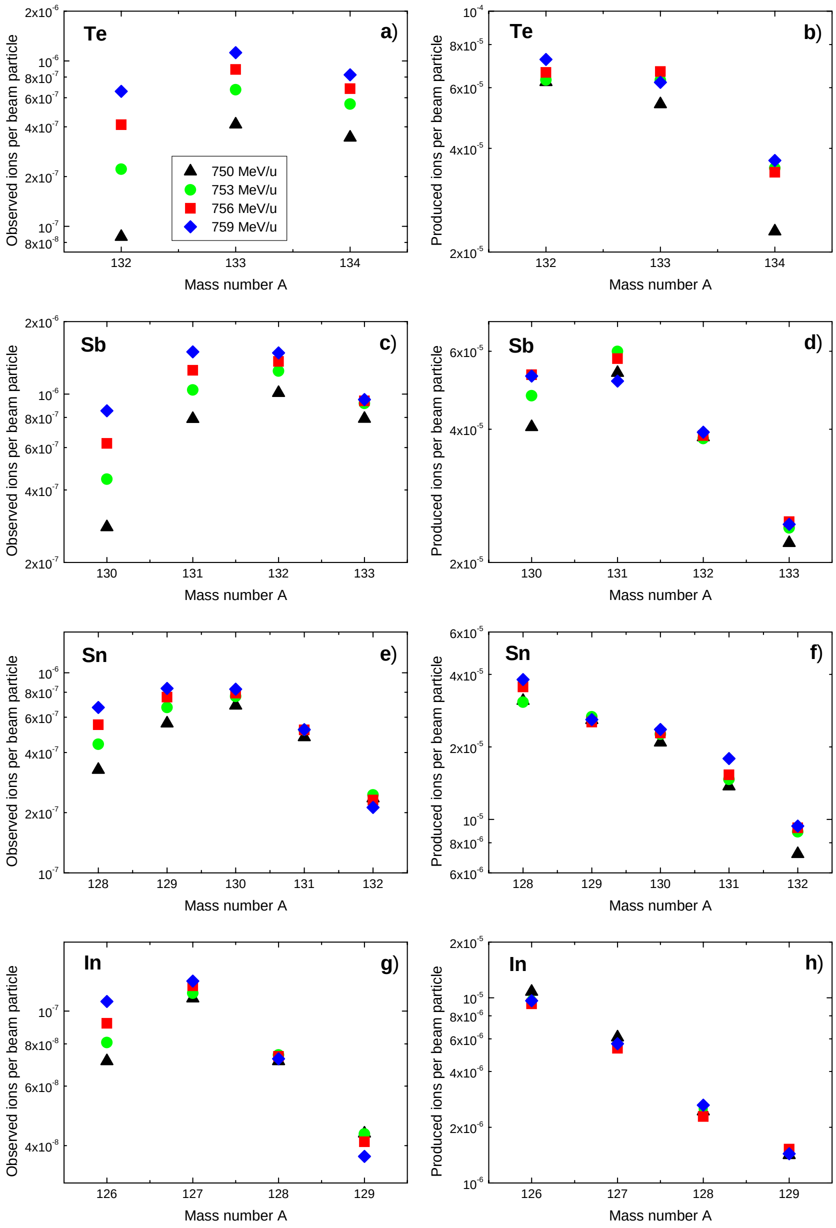

Figure 6.10: Observed and production rates measured during the momentum distribution scan (Experiment III.b). All data is measured with a Be target during setting optimized for ^{130}Sn.

Chapter 7

Conclusions and outlook

Projectile fragmentation and in-flight fission of relativistic heavy ions are highly successful mechanisms for producing secondary radioactive nuclear beams of exotic nuclei. The combination of a fragment separator with an array of germanium detectors mounted at the final focal plane of the spectrometer is a powerful tool for spectroscopic studies of nuclear systems at the limits. The separator allows for in-flight event-by-event identification of the selected exotic ions. In this way previously inaccessible areas of the nuclidic chart have been opened up for γ-ray spectroscopy. In four experiments performed at the Fragment Separator at GSI, using this technique, we searched for isomeric states in the neutron-rich Hf/W/Os isotopes, and in the vicinity of the doubly-magic nucleus ^{132}Sn. We have found a number of new isomers extending the experimental knowledge towards the neutron-rich side of the nuclidic chart. The angular momentum population in relativistic fission was investigated in terms of isomeric ratios measured for 9 isomers with angular momenta between 5 and 25/2 units of $\hbar$. The production rates for most of the isotopes observed during Experiment III with Be and Pb targets were evaluated.

Still many questions remain open and from the spectroscopic information obtained for neutron-rich neighbours of ^{132}Sn, as well as in the Hf/W/Os region, it is clear that further studies of the evolution of low-lying single-particle and collective excitations as a function of the neutron number is needed. The preliminary isomeric ratios for ^{129}Sn, ^{129}In and ^{127}In need more experimental input (e. g. transition multipolarities, and the observation of the primary transition in ^{127}In) to calculate the final results.

The information from a purely technical point of view provided from these experiments and the experience gained in the course of them is also an important issue, which is very helpful in the process of designing and the development of new radioactive nuclear beam facilities.

Bibliography

[1] C.N. Davids *et al.*, Phys. Rev. Lett. **76**, (1996) 592.

[2] "An International Accelerator Facility for Beams of Ions and Antiprotons", GSI conceptual design report, November 2001

[3] W. Nazarewicz, JYFL Summer School, Jyväskylä, Finland, 1999

[4] H. Simon *et al.*, Phys. Rev. Lett. **83**, (1999) 496.

[5] A. Navin *et al.*, Phys. Rev. Lett. **85**, (2000) 266.

[6] M. Bernas *et al.*, Phys. Lett. B **331**, (1994) 19.

[7] R. Grzywacz *et al.*, Phys. Rev. C **55**, (1997) 1126

[8] T. Suzuki *et al.*, Phys. Rev. Lett. **75**, (1995) 3241.

[9] J. Dobaczewski, I. Hamamoto, W. Nazarewicz, and J.A. Sheikh, Phys. Rev. Lett. **72**, (1994) 981.

[10] T. Werner *et al.*, Z. Phys. A **358**, (1997) 169.

[11] J. Dobaczewski, W. Nazarewicz, T.R. Werner, J.F. Berger, C.R. Chinn, and J. Dechargé, Phys. Rev. C **53**, (1996) 2809.

[12] H. Morinaga, T. Yamazaki, "In-beam gamma-ray spectroscopy", North-Holland publishing company, 1976

[13] K.E. G. Löbner, *et al.*, Phys. Lett. B **26**, (1968) 369.

[14] P.M. Walker and G.D. Dracoulis, submitted to Hyperfine Interactions.

[15] S. Åberg, Nucl. Phys. A **306**, (1978) 89.

[16] K. Jain, *et al.*, Nucl. Phys. A **591**, (1995) 61.

[17] J. Blomqvist, *Proc. of the 4th International Conference on Nuclei Far From Stability,* Helsingör 1981, (Report No. 81-09, CERN, Geneva, 1981), p. 536

[18] J.P. Omtvedt, Ph.D. thesis, University of Oslo (1995).

[19] H. Grawe and M. Lewitowicz, Nucl. Phys. A **693**, (2001) 116.

[20] N. Bohr and F. Kalckar, Det Kgl. Danske Videnskabernes Selskab, Mathematisk-fysiske Meddelelser **XIV**, 10, København, Levin and Munksgaard, 1937.

[21] R. Pfaff, Ph.D. thesis, Michigan State University (1996).

[22] R. Serber, Phys. Rev. **72**, (1947) 1114.

[23] P. Armbruster *et al.*, Z. Phys. A **355**, (1996) 191.

[24] Ch.O. Engelmann, Ph. D. thesis, Universität Tübingen, DISS.98-15, July 1998.

[25] H. Geissel *et al.*, Nucl. Instr. Meth. B **70**, (1992) 286.

[26] Ch. Schlegel *et al.*, Physica Scripta T **88**, (2000) 72.

[27] C. Ziegler *et al.*, Sci. Rep. GSI-91-1, (1991) p.291.

[28] G. Münzenberg, Nucl. Instr. and Meth. **B 70**, (1992) 265.

[29] M. Steiner, Diplomarbeit, TH Darmstadt (1991).

[30] M. Pfützner, B. Voss, H.-G. Clerc, H. Geissel, G. Münzenberg, F. Nickel, K.-H. Schmidt, M. Steiner, K. Sümmerer, and D.J. Vieira, Sci. Rep. GSI-91-1, (1991) p. 288.

[31] M. Hausmann *et al.*, Nucl. Instr. and Meth. **A 446**, (2000) 569.

[32] T. Aumann, P.F. Bortignon, H. Emling, Annu. Rev. Nucl. Part. Sci. **48**, (1998)

[33] N. Iwasa, H. Geissel, G. Münzenberg, C. Scheidenberger, Th. Schwab, and H. Wollnik, Nucl. Instr. Meth. B **126**, (1997) 284.

[34] C. Scheidenberger and H. Geissel, Nucl. Instr. Meth. B **135**, (1998) 25.

[35] J. Simpson *et al.*, Heavy Ion Phys. Res. II, (2000) p. 159

[36] http://www-aix.gsi.de/∼wolle/VEGA_EUROBALL/HTML/vega_project.html

[37] http://www-w2k.gsi.de/frs/technical/daq/frs-algorithms.asp

[38] C. Scheidenberger, Th. Stöhlker, W.E. Meyerhof, H. Geissel, P.H. Mokler, and B. Blank, Nucl. Instr. Meth. B **142**, (1998) 441.

[39] http://www-aix.gsi.de/∼wolle/EB_at_GSI/main.html

[40] J. Kantele, “Handbook of nuclear spectrometry”, Academic Press, Harcourt Brace and Company 1995.

[41] M. Mineva *et al.*, to be published.

[42] http://www.nndc.bnl.gov/nndc/physco/

[43] M. de Jong *et al.*, Nucl. Phys. A **613**, (1997) 435.

[44] M. Pfützner *et al.*, Phys. Lett. B**444**, (1998) 32.

[45] P.M. Walker *et al.*, Nucl. Phys. A **568**, (1994) 397.

[46] G.D. Dracoulis and P.M. Walker, Nucl. Phys. A **342**, (1980) 335.

[47] C.J. Pearson *et al.*, Phys. Rev. Lett. **79**, (1997) 605.

[48] M. Caamaño *et al.*, Acta. Phys. Pol. B **32**, (2001) 763.

[49] J. Benlliure *et al.*, Nucl. Phys. A **660**, (1999) 87.

[50] B. Fogelberg, H. Mach, H. Gausemel, J.P. Omtvedt and K.A. Mezilev, AIP Conference Proceedings **447**, 75 (1998).

[51] B. Fogelberg, in *Procedings of the International Conference on Nuclear Data in Science and Technology*, Mito, Japan, (1988) p. 837.

[52] J. Genevey *et al.*, Phys. Rev. C **67**, (2003) 054312.

[53] J. Genevey, J. A. Pinston, C. Foin, M. Rejmund, H. Faust and B. Weiss, Phys. Rev. C **65**, (2002) 034322.

[54] B. Fogelberg *et al.*, Nucl. Phys. A**352**, (1981) 157.

[55] J.P. Omtvedt, H. Mach, B. Fogelberg, D. Jerrestam, M. Hellström, L. Spanier, K.I. Erokhina, and V.I. Isakov, Phys. Rev. Lett. **75**, (1995) 3090.

[56] C.Y. Wu *et al.*, Nucl. Phys. A **607**, (1996) 178.

[57] C. Wheldon *et al.*, Nucl. Phys. A **652**, (1999) 103.

[58] R.F. Casten, "Nuclear Structure from a Simple Perspective", Oxford University Press, Oxford 1990.

[59] R.F. Casten, *et al.*, Phys. Rev. Lett. **47**, (1981) 1433.

[60] F. Xu *et al.*, Phys. Lett. B **435**, (1998) 257.

[61] J.A. Cizewski and E. Gülmez, Phys. Lett. B **175**, (1986) 11.

[62] H. Mach, Phys. Lett. B **185**, (1987) 20.

[63] P. Hoff, J.P. Omtvedt, B. Fogelberg, H. Mach, and M. Hellström, Phys. Rev. C **56**, (1997) 2865

[64] P. Alexa and R. Sheline, Phys. Rev. C **56**, (1997) 3087.

[65] M. Hellström *et al.*, in *Proceedings of the Third International Conference on Fission and Neutron-Rich Nuclei*, Sanibel Island, USA, Nov. 3-8, 2003 (World Scientific, 2004).

[66] M. Hellström *et al.*, work in progress.

[67] H. Gausemel, B. Fogelberg, T. Engeland, M. Hjorth-Jensen, P. Hoff, H. Mach, K.A. Mezilev and J.P. Omtvedt, Phys. Rev. C **69**, (2004) 054307.

[68] P. Hoff, B. Ekström, H. Göktürk and B. Fogelberg, Nucl. Phys. **A459**, (1986) 35.

[69] H. Göktürk, B. Ekström, E. Lund and B. Fogelberg, Z. Phys. **A324**, (1986) 117.

[70] L. Spanier, K. Aleklett, B. Ekström and B. Fogelberg, Nucl.Phys. **A474**, (1987) 359.

[71] C.T. Zhang *et al.*, Phys. Rev. C **62**, (2000) 057305.

[72] B. Fogelberg *et al.*, Nucl. Phys. **A323** (1979) 205.

[73] L.-E. De Geer and G.B. Holm, Phys. Rev. C **22**, (1980) 2163.

[74] S.K. Saha *et al.*, Phys. Rev. C **65**, (2002) 017302.

[75] P.J. Daly *et al.*, Z. Phys. A **358**, (1997) 203.

[76] W. Urban *et al.*, Phys. Rev. C **62**, (2000) 027301.

[77] J. Genevey *et al.*, EPJ A**7**, (2000) 463.

[78] J. Genevey *et al.*, EPJ A**9**, (2000) 191.

[79] B. Fogelberg *et al.*, Phys. Lett. B**209**, (1988) 173.

[80] P. Bhattacharyya *et al.*, Phys. Rev. Lett. **87**, (2001) 062502.

[81] J.A. Pinston *et al.*, Phys. Rev. C **61**, (2000) 024312.